PAPER

Check for updates

Fabrication and characterization of Cu–ZnO–cellulose acetate electrospun nanocomposite membranes for dual-function photocatalytic degradation and microbial inhibition

Hasitha Herath, [a] Viduranga Pasindu, [b] Piumika Yapa, [b] Sanduni Dabare, [b] Imalka Munaweera, *[b] Manjula M. Weerasekera [c] and Upeka Samarakoon [d]

Antimicrobial resistance is a growing global health threat, motivating the design of materials with enhanced, broad-spectrum antimicrobial performance under practical conditions. Zinc oxide (ZnO) nanoparticles are attractive for their intrinsic antimicrobial activity, but their photocatalytic efficacy is typically limited to UV irradiation due to a wide band gap. Here, Cu-doped ZnO ($Cu_xZn_{100-x}O$) nanohybrids were synthesized *via* co-precipitation with varying Cu contents (x = 0, 3, 5, 7, 10) and calcination temperatures (450 °C and 650 °C) to enable visible-light activation and synergistic antimicrobial activity. XRD, FTIR, SEM-EDX, UV-vis DRS, and AAS analyses confirmed the successful incorporation of Cu, along with corresponding changes in morphology and band gap modulation. The 7% Cu-doped ZnO prepared at 450 °C exhibited the lowest band gap and the highest photocatalytic activity toward methylene blue under visible light, alongside the strongest antioxidant capacity (IC_{50} = 151 µg mL^{-1}). Antimicrobial activity assessed by agar well diffusion demonstrated superior inhibition zones for 7% Cu–ZnO compared to pure ZnO across gram-positive (*Staphylococcus aureus*, MRSA), gram-negative (*Escherichia coli*, *Salmonella typhi*, *Shigella sonnei*), and fungal (*Candida albicans*) strains. Cu doping markedly enhanced the antimicrobial performance of ZnO nanofiber mats. The 7% Cu–ZnO mats exhibited significantly larger inhibition zones against both Gram-positive and Gram-negative bacteria as well as *C. albicans* compared to pure ZnO mats, confirming their superior broad-spectrum activity. 7% Cu-doped ZnO processed at 450 °C functions as a visible-light-active, broad-spectrum antimicrobial nanohybrid, and its incorporation into cellulose acetate nanofibers provides a cost-effective, scalable membrane platform for advanced antimicrobial and photocatalytic applications.

1. Introduction

A light-driven process in which a semiconductor catalyst absorbs photons generates electron–hole pairs that trigger chemical reactions. This method has attracted significant interest for environmental applications, as it directly harnesses abundant solar energy to break down pollutants into harmless products.[1] Photocatalytic materials can degrade organic pollutants or neutralize microorganisms, turning them into harmless compounds like CO_2 and H_2O. This sunlight-driven process provides an eco-friendly and sustainable approach to water purification, efficiently removing contaminants while addressing critical environmental and energy challenges.[2]

The performance of a photocatalyst depends strongly on its nanostructure. Nanoscale catalysts demonstrate significantly higher activity than their bulk counterparts, owing to quantum size effects and their exceptionally high surface-to-volume ratios.[3] In nanoscale particles, the confinement of electrons and holes leads to enhanced redox potentials, facilitating their rapid migration to the surface. At the surface, these charge carriers generate reactive oxygen species (ROS), which effectively participate in oxidation–reduction reactions. This spatial separation reduces charge-carrier recombination, thereby accelerating photocatalytic surface reactions and improving overall catalytic efficiency.[4] Accordingly, modern strategies to boost photocatalytic efficiency often rely on nanostructuring and compositing, such as doping with metal ions, forming

[a] *College of Chemical Sciences, Institute of Chemistry Ceylon, Rajagiriya, CO (10107), Sri Lanka. E-mail: hasithaherath351@gmail.com*

[b] *Department of Chemistry, Faculty of Applied Sciences, University of Sri Jayewardenepura, Nugegoda (10250), Sri Lanka. E-mail: imalka@sjp.ac.lk, pasinduviraj8@gmail.com, piumikayapa@gmail.com, dabaresanduni@gmail.com*

[c] *Department of Microbiology, Faculty of Medical Sciences, University of Sri Jayewardenepura, Nugegoda (10250), Sri Lanka. E-mail: mmweera@sjp.ac.lk*

[d] *Department of Nano Science Technology, Faculty of Technology, Wayamba University of Sri Lanka, Kuliyapitiya (60200), Sri Lanka. E-mail: upeka@wyb.ac.lk*

heterojunctions or coupling with co-catalysts.[5] These modifications extend light absorption and further improve charge separation, enabling much faster pollutant degradation.

Zinc oxide (ZnO) is one of the most studied photocatalysts thanks to its strong oxidation power, chemical stability, and low cost.[6] ZnO possesses a wide band gap ($\sim$3.2–3.4 eV) and a high exciton binding energy ($\sim$60 meV), enabling efficient generation of superoxide and hydroxyl radicals under UV irradiation. Its biocompatibility and natural abundance have driven widespread applications in sensors, solar cells, and photocatalysis. However, the wide band gap confines ZnO activity to the UV portion of the solar spectrum ($\sim$5–7% of total solar energy), and its photogenerated electrons and holes are prone to rapid recombination, limiting overall photocatalytic efficiency.[6] These limitations constrain ZnO's practical efficiency under sunlight, driving efforts to enhance its visible-light activity through strategies such as metal-ion doping, formation of heterojunctions, and incorporation into nanostructured composites. A well-established strategy to enhance ZnO's photocatalytic performance is doping with transition metals. In particular, substituting Cu^{2+} ions into the ZnO lattice significantly modifies its optoelectronic properties. Cu incorporation introduces defect states and intermediate energy levels, effectively narrowing the band gap and extending light absorption into the visible region.[7] At the same time, the Cu dopant creates surface states that favor the generation of oxidative species and trap charge carriers to slow recombination. Consequently, Cu–ZnO composites exhibit significantly enhanced photocatalytic degradation of dyes and pollutants compared to pure ZnO. Even low atomic percentages of Cu can markedly accelerate the photodegradation of rhodamine B, enabling near-complete mineralization under UV/visible light, whereas unmodified ZnO shows substantially slower degradation rates.[7]

Importantly, Cu–ZnO hybrids also exhibit strong antimicrobial effects. Both ZnO and copper ions are known to be toxic to bacteria *via* the generation of reactive oxygen species and disruption of cell membranes. Studies have shown that Cu-incorporated ZnO coatings can completely eliminate bacterial colonies in a short time. For instance, transparent Cu–ZnO films achieved total inactivation of *E. coli* under hospital-type white light within 6 hours, and even in the dark (24 h) for higher Cu content.[8] This strong biocidal activity is attributed to multiple concurrent mechanisms, including the generation of reactive oxidative species and the release of Cu^{2+} ions, which together overwhelm microbial defense systems. Consequently, Cu–ZnO nanocomposites function as effective broad-spectrum antimicrobial agents in addition to their photocatalytic properties.[9,10]

To harness the advantages of these nanomaterials in practical applications, an effective strategy is to incorporate Cu–ZnO nanoparticles into a polymer matrix at greater loading. Electrospinning cellulose acetate (CA) produces fibrous mats with high surface area, facilitating maximal exposure of the immobilized catalysts to water. Such nanofiber–nanoparticle composites have been demonstrated to function effectively as filtration membranes and for pollutant degradation.[11] In particular, incorporating functional nanoparticles into CA fibers can impart additional properties: CA is biocompatible and easily processable, and embedding bioactive particles (*e.g.*, Ag, Cu, ZnO) produces versatile antimicrobial membranes.[11] For example, ZnO nanoparticles in CA nanofibers retain their photocatalytic and antimicrobial activity, making the composite useful for water disinfection and dye degradation.[12] In essence, a CA–Cu–ZnO nanohybrid membrane integrates the mechanical integrity and hydrophilicity of the polymeric support with the visible-light-driven oxidative capability and broad-spectrum biocidal activity of Cu–ZnO nanoparticles. Building on these principles, the present study focuses on the fabrication and systematic evaluation of CA nanofiber membranes loaded with Cu–ZnO nanostructures, aiming to achieve synergistic solar-driven photocatalysis and microbial disinfection for advanced multifunctional applications. As illustrated in Fig. 1, this study represents the first focused investigation into the sterilizing capabilities of cellulose acetate-based Cu–ZnO nanofiber membranes under visible light irradiation.

2. Materials and methods

2.1 Materials and reagents

All reagents, metal precursors, and other chemicals, including zinc acetate dihydrate, copper chloride, sodium hydroxide (NaOH), polyethyleneglycol 12 000 (PEG_{12000}), methylene blue, 2,2 diphenyl-1-picrylhydrazyl (DPPH), methanol, ascorbic acid, acetone, dimethylformamide, cellulose acetate, sodium chloride (NaCl), barium chloride ($BaCl_2$), and sulfuric acid (H_2SO_4) were obtained from Sigma Aldrich, USA. Chemicals, media, and other materials for microbiology research, such as nutritional agar, Muller Hinton agar, Muller Hinton broth agar, bacteriological agar, blood agar, and antibiotic powders were obtained from HiMedia in India. ATCC strains of *Staphylococcus aureus* (ATCC 25923), *Shigella sonnei* (ATCC 25931), *Escherichia coli* (ATCC 25922), *Salmonella typhi* (ATCC 6539), and *Candida albicans* (ATCC 12031) were obtained from the Department of Microbiology, University of Sri Jayewardenepura, Sri Lanka.

2.2 Synthesis and characterization of ZnO and Cu–ZnO nanoparticles

In 50 mL of deionized water, 5.30 g of zinc acetate dihydrate was dissolved. After the addition of 1.00 g of PEG_{12000}, 2 M NaOH was drop wisely added while being constantly stirred until the pH of the mixture reached about 12. After two hours of stirring the reaction mixture, the resulting gel was centrifuged and given three rounds of washing with deionized water. After that, the precipitate was oven dried for 12 hours at 100 °C. Zinc oxide nanoparticles were calcined for two hours at 450 °C. The calcined ZnO nanoparticles were further ground with a mortar and pestle to produce the fine powder.

To synthesize the Cu doped ZnO, the zinc acetate dihydrate solution was prepared by dissolving 10.15 g of zinc acetate in 50 mL of deionized water. A copper chloride solution was prepared by mixing 0.2377 g of copper chloride in 30 mL of deionized water. Both solutions were mixed at once. PEG_{12000} was added to that solution followed by the dropwise addition of
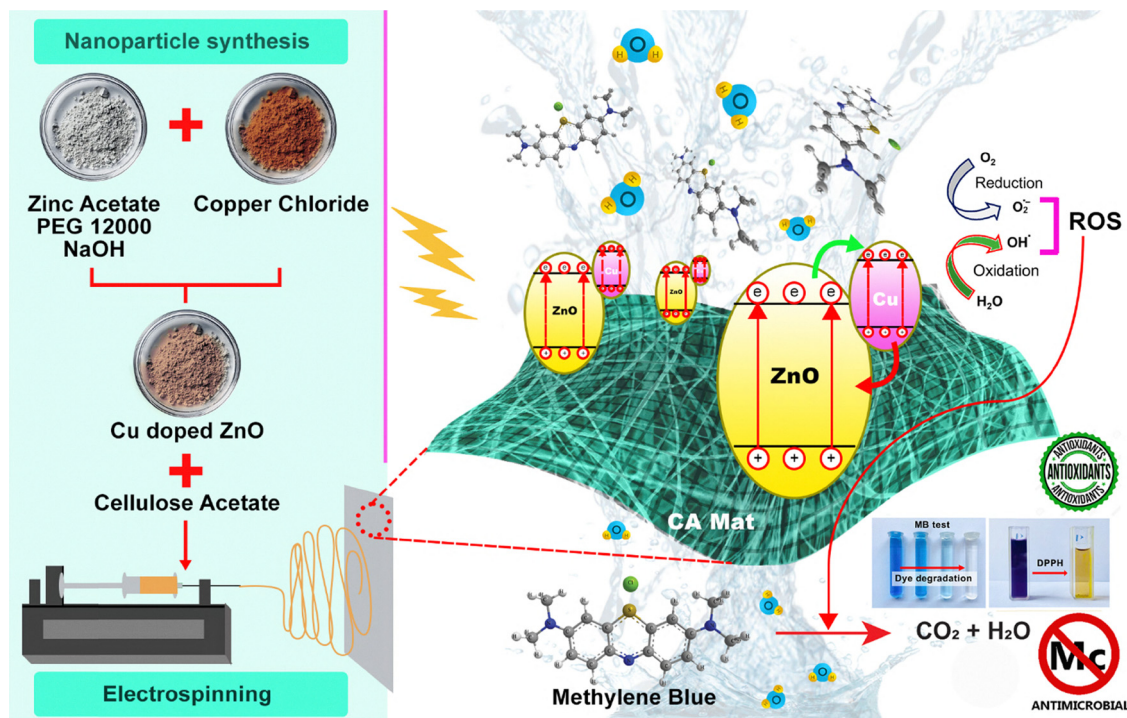
Fig. 1 Research design.

2 M NaOH. The reaction mixture was stirred for 2 hours and the resultant gel was centrifuged and washed with deionized water three times. The precipitates were collected, and dried at 100 °C for 12 hours using an oven. The oven dried product was calcined at 450 °C for 2 hours to obtain Cu 3%–ZnO nanohybrid. The aforementioned procedure was followed to obtain 5% Cu–ZnO, 7% Cu–ZnO and 10% Cu–ZnO nanohybrids using 0.3959 g, 0.56 g, and 0.817 g copper chloride, respectively.[13,14]

To investigate the impact of calcination temperature on the structural and functional characteristics, a parallel batch of nanohybrids with the same compositional ratios was calcined at 650 °C using the identical synthesis procedure. This comparative study allowed for the assessment of temperature effects on crystallinity, particle size, band gap, and photocatalytic and antimicrobial performance of the synthesized nanoparticles. The crystalline structures of the synthesized nanohybrids were analyzed by powder X-ray diffraction (PXRD; Rigaku SmartLab, 3 kW sealed X-ray tube, CBO optics, D/teX Ultra 250 silicon strip detector). Functional groups and characteristic peaks were examined using Fourier-transform infrared (FTIR) spectroscopy with the KBr pellet method (Bruker Vertex 80). Optical band gaps were determined from diffuse reflectance UV-vis spectroscopy (Perkin-Elmer UV Express, version 4.1.3). Morphological features were studied via scanning electron microscopy (SEM; ZEISS, secondary electron mode, 10 kV), and surface elemental composition was analyzed by energy-dispersive X-ray spectroscopy (EDX).

2.3 Evaluation of the photocatalytic activity of nanohybrids

The photocatalytic activity of pure ZnO and Cu–ZnO nanohybrids was determined by observing the degradation of a methylene blue (MB) dye solution. About 350 μL methylene blue was taken into a 500 mL volumetric flask and it was topped up with distilled water to make the stock MB solution. Then 10 mL of prepared methylene blue solution from the stock solution and 20 mg of catalyst were mixed, and the samples were kept in the dark for one hour, to reach the adsorption desorption equilibrium. A photodegradation experiment was carried out under sunlight (intensity 45–75 Klux) and dark conditions while continuously stirring the solutions using magnetic stirrer for 90 minutes.[15] After every 10 minutes time interval, aliquots (5 mL) were extracted and centrifuged. The photocatalytic degradation of methylene blue was monitored over time using UV-vis spectroscopy, measuring the absorbance at 663 nm.[16]

2.4 Evaluation of the antimicrobial activity of synthesized nanohybrid powders

ZnO and Cu–ZnO nanohybrids (450 °C) were tested against the ATCC cultures of including both gram-positive (*Staphylococcus aureus* and MRSA) and gram-negative bacteria (*Escherichia coli*, *Salmonella typhi*, *Shigella sonnei*), as well as the fungus *Candida albicans*. These microorganisms are predominant pathogenic microbes that can be commonly observed in humans. Commercially available antibiotics: erythromycin (100 μg) was used as the positive control for gram-positive bacteria. Gentamycin (100 μg) was used for gram-negative bacteria, and fluconazole (100 μg) was used for *Candida albicans*.

The prepared media and tips of the micropipette were sterilized in an autoclave at 121 °C (15 bar pressure) for 15 minutes. Other glassware was sterilized in a hot air oven

at 160 °C for 2 hours. A quantity of 25 mL of Muller Hinton agar was poured into each disposable Petri dish and allowed to solidify. Then suspensions of all the selected microorganisms were prepared, which were adjusted with their concentrations to 0.5 McFarland's standard (10^8 CFU mL^{-1}). Then 100 μL from each inoculum was pipetted out and cultured on the solidified agar plates by using the streak plate method. Then wells were cut using sterile pipette tips and sealed at the bottom by placing 1–2 drops of MHA. Then it was allowed to dry to obtain the sealed wells. The metallic dispersions were then pipetted to the respective well (100 μL from each dispersion of metallic nanohybrid that has a concentration of 100 mg mL^{-1}), and all the agar plates were incubated for 24 hours at 37 °C. Finally, the zone of inhibition (ZOI) around each well is measured in millimeters by using a zone reader (Netillin Zone Reader, USA). Each experiment is performed in triplicate ($n = 3$), and the mean value is calculated.

2.5 Determination of radical scavenging activity and IC$_{50}$ values of ZnO and 7% Cu–ZnO nanohybrids by DPPH assay

The (DPPH assay method was used to measure the nanohybrids' capacity to scavenge free radicals, and the IC$_{50}$ value was computed. After dispersing 1 mL of nanohybrid solution at various concentrations in distilled water, precisely 1 mL of 100 μM DPPH produced in methanol was added. The standard used was ascorbic acid (0.1 M). At 517 nm, absorbance was measured, and the following eqn (1) was used to determine the DPPH scavenging activity.

$$\text{DPPH scavenging activity} = \frac{(A_0 - A_t)}{A_0} \times 100\% \qquad (1)$$

where A_0 is the absorbance of the stock DPPH solution, A_t is the absorbance of the sample mixture.[13,17]

2.6 Fabrication and characterization of pure ZnO and 7% Cu–ZnO nanohybrids incorporated electrospun cellulose acetate (CA) nanofibers

2.6.1 Preparation of 40% (w/w) pure ZnO (450 °C) embedded nanofiber mat.
To prepare the electrospinning solution, 600 mg of cellulose acetate (CA) was weighed and transferred into a glass vial. A solvent mixture of acetone and N,N-dimethylformamide (DMF) in a 2 : 1 volume ratio (4 mL of acetone and 2 mL of DMF) was added to the vial. The solution was stirred for 1 hour to ensure complete dissolution of the polymer. Subsequently, 400 mg of pure ZnO nanoparticles calcined at 450 °C were added to the polymer solution to achieve a 40% (w/w) ZnO loading in the CA matrix. The mixture was then stirred continuously for 6 hours to promote uniform dispersion of the nanoparticles, followed by sonication for 30 minutes to eliminate agglomeration and ensure homogeneity. The final polymer–nanoparticles solution was loaded into a syringe equipped with a needle. Electrospinning was conducted for 5 h at 19 kV, 1.5 mL h^{-1} flow rate, and a 13 cm needle-to-collector distance, with aluminum foil on the collector to collect the nanofibers.[13,17] The process was conducted at temperature of 32 °C and humidity of 60%.[15]

2.6.2 Preparation of 40% (w/w) 7% Cu–ZnO (450 °C) embedded nanofiber mat.
An amount of 600 mg of cellulose acetate (CA) was weighed and placed into a glass vial. A solvent mixture of acetone and N,N-dimethylformamide (DMF) in a 2 : 1 volume ratio (4 mL acetone and 2 mL DMF) was added, and the mixture was stirred for 1 hour to dissolve the polymer. To this solution, 400 mg of 7% Cu-doped ZnO nanohybrid calcined at 450 °C were incorporated to achieve a 40% (w/w) loading of nanohybrids within the CA matrix. The nanoparticle–polymer suspension was stirred for 6 h, sonicated for 30 min, and electrospun for 5 h at 19 kV, 1.5 mL h^{-1}, and 13 cm needle-to-collector distance, with aluminum foil on the collector, under 32 °C and 60% humidity.

2.6.3 Characterization of pure ZnO and 7% Cu–ZnO nanohybrids incorporated electrospun cellulose acetate (CA) nanofibers.
The crystalline structures of the prepared nanofiber mats were analyzed using powder X-ray diffraction (PXRD), allowing identification of phase purity and crystallinity. To investigate the presence of functional groups and bonding characteristics, Fourier transform infrared spectroscopy (FTIR) was performed in ATR mode. The surface morphology and fiber distribution of the electrospun membranes were examined using scanning electron microscopy (SEM). To assess the elemental dispersion and confirm the homogeneous incorporation of Cu and Zn throughout the nanofiber mats, atomic absorption spectroscopy (AAS) was employed. Prior to analysis, samples were digested using a manual acid digestion method. A 100 cm^2 section of the electrospun membrane was selected from which 1 cm^2 samples were collected from the center and each corner. Triplicate samples from each location were digested in a 3 : 1 HCl–HNO$_3$ mixture at 95 °C for 2–3 h under a fume hood. The filtered solutions were analyzed by AAS to quantify metal content and confirm uniform distribution.

2.6.4 Photocatalytic and free radical scavenging activity of ZnO and 7% Cu–ZnO nanohybrid–loaded CA nanofiber membranes.
The photocatalytic activity of cellulose acetate (CA) fiber mats incorporated with pure ZnO and 7% Cu–ZnO nanohybrids was evaluated by analyzing the degradation of methylene blue (MB) dye under visible light. A 1 cm^2 portion of each membrane sample was immersed in 10 mL of methylene blue solution and kept in the dark for 1 hour to achieve adsorption–desorption equilibrium. After this, the photodegradation experiment was conducted under visible light and dark conditions, while continuously stirring the solution with a magnetic stirrer for 60 minutes. At 10 minutes intervals, 5 mL aliquots were withdrawn, centrifuged, and their absorbance was measured using UV-vis spectroscopy, with particular attention to the 663 nm peak of methylene blue. The degradation percentage over time was calculated based on the reduction in absorbance at this wavelength.

To evaluate the free radical scavenging ability, a DPPH assay was performed. A 5 cm^2 section of each fiber mat was placed in a test tube containing 1 mL of distilled water and 1 mL of 0.1 mM DPPH solution prepared in methanol. The mixture was shaken well and kept in the dark for 30 minutes, after which the absorbance was recorded at 517 nm using UV-vis

spectroscopy. The percentage of DPPH radical scavenging was calculated using the standard formula. All tests were conducted in triplicate using separate portions of each sample to ensure reproducibility and statistical relevance.

2.7 Evaluation of the antimicrobial activity of ZnO nanoparticles and 7% Cu–ZnO nanohybrid incorporated electrospun CA membranes

The disc diffusion method was conducted to observe the antimicrobial activity of the ZnO and Cu nanohybrid incorporated electrospun polymer membranes. ZnO and 7% Cu–ZnO nanohybrid incorporated electrospun membranes were tested against the ATCC cultures of including both gram-positive (*Staphylococcus aureus* and MRSA) and gram-negative bacteria (*Escherichia coli*, *Salmonella typhi*, *Shigella sonnei*), as well as the fungus *Candida albicans*, all of which are known to cause human infections. Commercially available antibiotic discs of erythromycin (15 μg) were used as the positive control for gram-positive bacteria. Gentamycin (10 μg) was used for gram-negative bacteria, and fluconazole (15 μg) was used for *Candida albicans*. Cellulose acetate electrospun membrane was used as the negative control. The diameter of the discs that were used for the assays was 6 mm.

As described in Section 2.4, the media were prepared and autoclaved, and bacterial and fungal suspensions were cultured on the plates. Fresh cultures of the specified microorganisms were used to prepare the suspensions. Sterile discs were placed on the surface of the solidified agar using sterile forceps, and the plates were incubated at 37 °C for 24 h. The zones of inhibition were then measured using a Netillin Zone Reader (USA). All experiments were performed in triplicate following CLSI guidelines.

3. Results and discussion

This study reports the fabrication and characterization of cellulose acetate (CA) electrospun nanofiber membranes embedded with Cu-doped ZnO nanohybrids, designed as visible-light-active, biodegradable, and self-sterilizing materials. ZnO, a wide band gap semiconductor with intrinsic photocatalytic and antimicrobial properties, was doped with Cu^{2+} ions to enhance charge separation, extend visible-light absorption, and improve overall redox performance. The substitutional incorporation of Cu^{2+} into the ZnO lattice was intended to modify the electronic structure while maintaining the intrinsic wurtzite crystal phase. Cu-doped ZnO nanoparticles were synthesized *via* a co-precipitation method with Cu doping concentrations of 0, 3, 5, 7, and 10 mol%, followed by calcination at 450 °C and 650 °C. These conditions were chosen to evaluate the effects of both doping level and thermal treatment on the structural, optical, and functional properties of the resulting nanohybrids. Optical properties were characterized using UV-vis diffuse reflectance spectroscopy (DRS), and band gap energies were estimated from Tauc plots. Cu incorporation induced a progressive red shift in the absorption edge relative to undoped ZnO, indicating enhanced visible-light absorption. Among the samples, 7% Cu–ZnO exhibited the lowest band gap values at both 450 °C and 650 °C calcination temperature. Calcined the photocatalytic efficiency of the lowest band gap nanohybrids was evaluated *via* the visible-light-driven degradation of methylene blue (MB) dye. Among all samples with varying Cu doping levels and calcination temperatures, the 7% Cu–ZnO nanohybrids calcined at 450 °C exhibited the highest photodegradation efficiency.

3.1 Characterization of the synthesized ZnO and Cu–ZnO nanohybrids

To confirm the successful synthesis and phase purity of Cu-doped ZnO nanohybrids, PXRD analysis was carried out for all synthesized samples. Fig. 2(a) presents the PXRD patterns of pure ZnO and Cu-doped ZnO nanoparticles with doping levels of 0%, 3%, 5%, 7%, and 10%, calcined at 450 °C and Fig. 3(a) presents the PXRD patterns of pure ZnO and Cu-doped ZnO nanoparticles with doping levels of 0%, 3%, 5%, 7%, and 10%, calcined at 650 °C. The calculated average crystallite sizes, unit cell parameters along with volumes for all doping concentrations
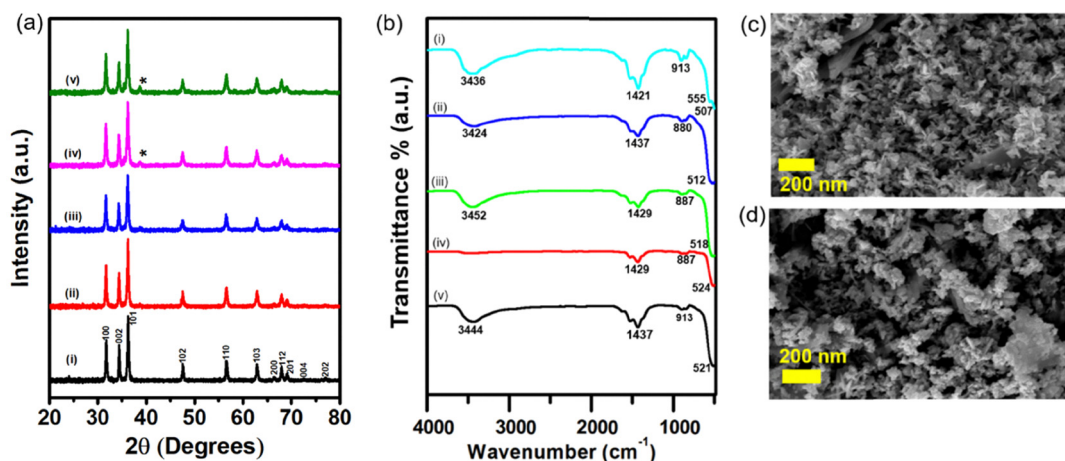

Fig. 2 (a) PXRD analysis and (b) FTIR analysis of 450 °C calcined samples (i). ZnO nanoparticles (ii). 3% Cu–ZnO nanoparticles (iii). 5% Cu–ZnO nanoparticles (iv). 7% Cu–ZnO nanoparticles (v). 10% Cu–ZnO nanoparticles. SEM image of 450 °C calcined (c) ZnO (d) 7% Cu–ZnO.
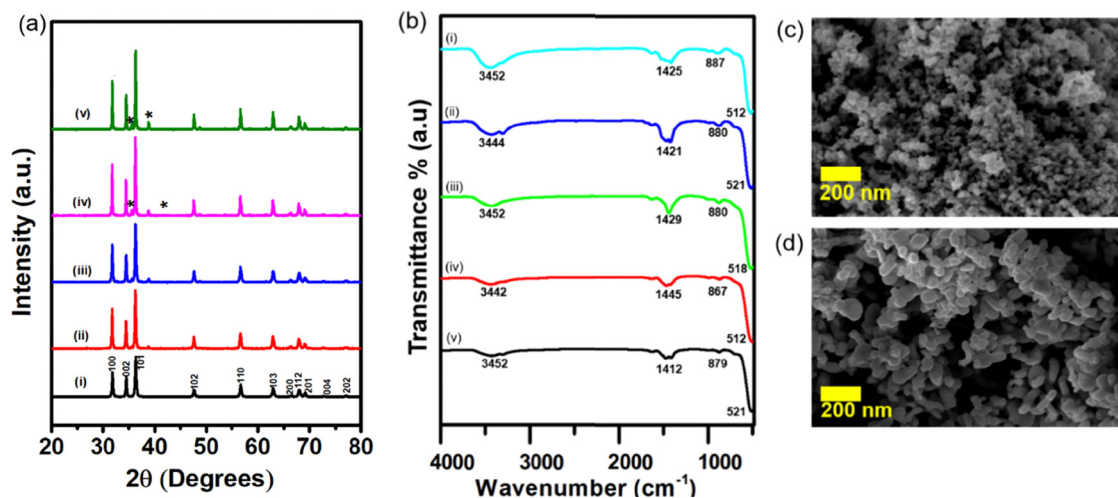
Fig. 3 (a) PXRD analysis (b) FTIR analysis of 650 °C calcined samples (i). ZnO nanoparticles (ii). 3% Cu–ZnO nanoparticles (iii). 5% Cu–ZnO nanoparticles (iv). 7% Cu–ZnO nanoparticles (v). 10% Cu–ZnO nanoparticles. SEM image of 650 °C calcined (c) ZnO (d) 7% Cu–ZnO.

Table 1 Average crystallite size of nanohybrids calcined at 450 °C

Sample	Average crystallite size (nm)	Unit cell parameters (Å) $a = b$	Unit cell parameters (Å) c	Volume (Å)^3
Pure ZnO	32.815	3.25	5.22	47.7479
3% Cu doped	30.207	3.25	5.22	47.7479
5% Cu doped	22.681	3.25	5.19	47.4735
7% Cu doped	19.954	3.26	5.23	48.1343
10% Cu doped	21.643	3.25	5.23	47.8394

Table 2 Average crystallite size of nanohybrids calcined at 650 °C

Sample	Average crystallite size (nm)	Unit cell parameters (Å) $a = b$	Unit cell parameters (Å) c	Volume (Å)^3
Pure ZnO	31.097	3.24	5.18	47.0909
3% Cu doped	35.004	3.25	5.20	47.5650
5% Cu doped	32.400	3.25	5.19	47.4735
7% Cu doped	53.559	3.25	5.20	47.5650
10% Cu doped	54.972	3.25	5.19	47.4735

and both calcination temperatures are summarized in Tables 1 and 2.

For the nanohybrids calcined at 650 °C and 450 °C, the diffraction peaks of the undoped ZnO sample were found to match well with the standard pattern for hexagonal wurtzite ZnO (JCPDS card no. 036-1451), with characteristic reflections assigned to the miller indices (100), (002), (101), (102), (110), (103), (200), (112), (201), (004), and (202) planes (Fig. 2(a) and 3(a)). The sharp and intense peaks confirm the high crystallinity of the synthesized material. The narrow width, sharpness, and high intensity of the diffraction peaks showed that ZnO as synthesized is a very pure, well defined crystalline nanomaterial. The average crystallite size of Cu-doped ZnO nanoparticles (Cu–ZnO NPs) was calculated using the following eqn (2), the Debye–Scherrer equation.

$$D = \frac{k\lambda}{\beta \cos \theta} \tag{2}$$

where D is the crystallite size, $k = 0.9$, λ is the X-ray wavelength ($\lambda = 0.154056$ nm), β is the diffraction peak's full width at half-minimum intensity (FWHM) on the 2θ scale measured in radians. A key observation from the average crystallite size calculated from PXRD data was the effect of both Cu doping concentration and calcination temperature on the average crystallite size. In the samples calcined at 450 °C, the average

crystallite size decreased progressively with increasing Cu content, the minimum crystal size was obtained at the 7% of Cu doping level and decreased above this again. In nanomaterials, a smaller crystallite size leads to a larger surface area-to-volume ratio, which provides more active sites for the reaction to undergo, therefore in semiconductor materials, increases the ROS generation and facilitating more efficient charge transfer and faster redox reactions under light irradiation. As a result, the 7% Cu–ZnO sample with the lowest crystallite size showed the highest photocatalytic degradation efficiency against methylene blue under visible light, clearly indicating that crystallite size plays a crucial role in optimizing the photocatalytic performance. This average crystallite size decreasing has been reported many times in the literature.[18–20] This reduction in grain size is attributed to the Zener pinning effect, whereby Cu^{2+} ions accumulate at grain boundaries and impede their motion. Acting either as substitutional or interstitial defects, Cu^{2+} dopants generate a retarding force on grain boundary migration, thereby stabilizing the microstructure and limiting grain coarsening.[21–23]

Grain growth in polycrystalline materials is driven by the reduction of grain boundary energy, which acts as the driving force for grain boundary migration. Dopant ions or second-phase particles can exert a pinning force (Zener pinning) at grain boundaries, which opposes this motion. When the pinning force exceeds the driving force, grain growth is

suppressed, resulting in smaller crystallite sizes. This pinning effect is more pronounced at lower calcination temperatures because the thermal energy available is insufficient to overcome the retarding force exerted by dopant segregation at grain boundaries, thereby effectively limiting grain coarsening.[22,23]

Conversely, in the samples calcined at 650 °C, an increase in average crystallite size was observed with increasing Cu doping which also has been reported many times.[24,25] At the higher calcination temperature of 650 °C, increased thermal energy enhances atomic mobility, promoting grain growth and partially offsetting the pinning effect of Cu dopants. Elevated temperatures also facilitate dopant diffusion and clustering, which can reduce lattice distortion and encourage crystallite coalescence. Consequently, although CuO impurities are present at higher doping levels in both temperature regimes, dopant-induced suppression of crystallite growth predominates at 450 °C, whereas grain growth is enhanced at 650 °C.[23]

The lattice parameters ($a = b$ and c) of Cu-doped ZnO samples were found to be similar to those of undoped ZnO, which can be attributed to the minimal ionic radius difference between Zn^{2+} and Cu^{2+} ions. Additionally, the c/a ratio was found to closely approach 1.633, indicative of an ideally close-packed hexagonal structure, which suggests that the wurtzite lattice remains structurally stable upon Cu doping.

The apparent stability of the unit cell parameters a, b, and c despite increasing Cu doping levels can be attributed to the close ionic radii of Cu^{2+} (0.73 Å) and Zn^{2+} (0.74 Å), which results in minimal lattice distortion upon substitution within the wurtzite ZnO structure. This allows the ZnO lattice to accommodate Cu ions without significant expansion or contraction of the lattice dimensions, maintaining a relatively constant unit cell volume.[26] Additionally, the presence of minor secondary phases such as CuO at higher doping concentrations may relax the lattice strain by segregating excess Cu outside the ZnO lattice, further stabilizing the bulk crystal parameters. Thus, despite compositional changes, the average lattice constants remain mostly unchanged, reflecting the structural resilience of ZnO to moderate Cu substitution.

In contrast, the variation in average crystallite size with doping and calcination temperature is governed primarily by microstructural factors such as grain boundary mobility and dopant segregation rather than changes in lattice parameters. At the lower calcination temperature (450 °C), Cu dopants tend to segregate at grain boundaries and exert a pinning effect (Zener pinning), which inhibits grain growth and reduces the average crystallite size as Cu content increases. Conversely, at the higher temperature (650 °C), enhanced atomic mobility enables grain coarsening and partial dopant diffusion or clustering, which can promote grain growth, leading to an increase in crystallite size with doping. This decoupling of crystallite size behavior from unit cell parameter changes is common in doped nanomaterials, where lattice constants reflect average atomic spacing but crystallite size depends on kinetic and thermodynamic factors controlling grain growth and defect formation.[26]

The unit cell volume calculated for ZnO and Cu–ZnO samples, exhibited no clear pattern of variation with increasing dopant concentration. This irregularity can be attributed to the complex structural responses of the ZnO lattice to Cu incorporation, which go beyond a straightforward ionic substitution mechanism. Although Cu^{2+} is closely matched in size with Zn^{2+}, the substitution of Zn^{2+} by Cu^{2+} does not uniformly alter the lattice dimensions due to several competing phenomena. At lower doping levels, Cu^{2+} ions likely substitute Zn^{2+} in the wurtzite lattice without inducing significant lattice distortion. However, as the dopant concentration increases, deviations from ideal substitution become more pronounced. Cu^{2+} ions may not only occupy substitutional sites but also enter interstitial positions or form nanoscale clusters, leading to local lattice distortions that are not homogeneously distributed throughout the crystal structure. Furthermore, the onset of secondary CuO phase formation at higher doping levels, even in small amounts, can relieve internal strain within the ZnO matrix and influence the effective lattice dimensions indirectly. Therefore strain relaxation mechanisms, such as bond angle distortions or point defect rearrangements may act to counterbalance the volumetric changes introduced by ionic substitution. Collectively, these factors contribute to the observed non-systematic behavior of the unit cell volume.[27]

The absence of a clear trend in structural parameters suggests that the ZnO lattice accommodates Cu incorporation through a combination of substitutional doping, defect-mediated relaxation, and microstructural adjustments, all while preserving its characteristic hexagonal wurtzite structure. This structural resilience underscores ZnO's ability to tolerate a wide range of dopant concentrations without undergoing significant crystallographic phase transitions.[28]

Even at higher Cu doping ratios and calcination temperatures, the crystal retains its hexagonal wurtzite structure, as shown by the stability of unit cell characteristics.[29,30] As shown in Fig. 2(a) and 3(a), the diffraction peaks widened as the material was doped with Cu ions from 3, 5, and 7, and 10 mol% respectively. As the molar ratio of the dopant increase, the degree of nano agglomeration also increased, as also confirm by SEM in Fig. 3(c).[31] For the Cu-doped ZnO samples, the main peaks corresponding to the wurtzite ZnO phase were preserved, indicating that the crystal structure remains predominantly ZnO. However, at higher percentages of Cu-doped ZnO samples exhibited additional diffraction peaks, which were absent in the undoped ZnO. These new peaks were analyzed and found to correspond to tenorite CuO (JCPDS card no. 048-1548), indicating the presence of a minor secondary CuO phase. This observation agrees with literature reports that at low Cu doping concentrations, Cu^{2+} ions can effectively substitute Zn^{2+} within the ZnO lattice due to their similar ionic radii. However, as the Cu content increases, excess Cu tends to segregate and crystallize as CuO, forming isolated clusters as an impurity phase.[13,32–34] This indicates that after a critical molar ratio, Cu–ZnO produces the separate CuO nano layer over ZnO NPs.[35]

Overall, these findings demonstrate that Cu doping critically influences crystallite size and phase purity, while the calcination temperature significantly affects the material's structural evolution. Notably, the 7% Cu-doped ZnO sample calcined at

450 °C exhibited the optimal combination of small crystallite size and high phase purity, which contributed to its superior photocatalytic and antimicrobial performance.[36,37]

The FTIR spectroscopy analysis was conducted to identify the functional groups, peak positions, and relevant peak shifts of the pure and Cu-doped ZnO nanohybrids calcined at 450 °C and 650 °C to further confirm the structure of nanohybrids. The spectra of all samples which shows in figure (Fig. 2(b) and 3(b)), revealed several key absorption bands that are characteristic of ZnO-based nanostructures, with notable variations observed upon doping and with changing calcination temperature. A broad and intense absorption band observed in the region of 3000–3500 cm^{-1} is attributed to the O–H stretching vibrations of surface hydroxyl groups and physically adsorbed water molecules. The peak around 1650 cm^{-1} corresponds to the bending vibration (H–O–H) of water molecules, further confirming the presence of adsorbed moisture across samples. In addition, peaks between range of 1630 and 1384 cm^{-1} were attributed to the asymmetric and symmetric stretching vibrations of carboxylate groups (COO$^-$), respectively.[38] These carboxylate groups are likely derived from residual carbon containing species used during synthesis.[39] As the crystallite size increases, the intensity of the FTIR peaks corresponding to surface-bound carboxylate and hydroxyl groups gradually diminishes, indicating a reduction in these surface functional groups. This trend is particularly evident in samples calcined at 650 °C, where increasing temperature promotes crystallite growth and reduces the surface-to-volume ratio, leading to a lower density of surface-active species.[40,41]

The most prominent peak of the FTIR spectra appears in the fingerprint region between 500 and 530 cm^{-1}, which corresponds to the Zn–O stretching vibrations in the ZnO wurtzite lattice.[42,43] In pure ZnO calcined at 450 °C, the Zn–O peak appears around 507 cm^{-1}. With increasing Cu doping concentration, minor peak shift to higher wavenumbers can be observed around 512 cm^{-1}, 518 cm^{-1}, 524 cm^{-1}, and 529 cm^{-1}. A similar trend was observed in the 650 °C samples, where the Zn–O peak appears near 512 cm^{-1} in the undoped ZnO and shifts up to 518 cm^{-1} upon doping which also has been reported many times.[44] The observed upward shift of the Zn–O stretching mode upon Cu incorporation aligns with established vibrational theory for mixed crystals. Because copper atoms (atomic mass ≈ 63.5 u) are slightly lighter than zinc atoms (atomic mass ≈ 65.4 u), their substitution into the ZnO lattice results in a slight increase in the frequency of the transverse optical phonon modes due to the reduced effective atomic mass in the bond.[45,46] Thus, the combined FTIR and PXRD analysis confirmed the successful integration of Cu^{2+} ions into the ZnO matrix, affirming both structural and vibrational modifications induced by doping.

The optical band gap energies (E_g) of undoped and Cu-doped ZnO nanohybrids were evaluated using UV-vis DRS, and the values were derived using Tauc plots by extrapolating the linear region of the $(F(R)h\nu)^2$ versus $h\nu$ plots to the $(F(R)h\nu)^2$ = 0 axis. Tauc plots for ZnO and Cu–ZnO nanohybrids calcined at 450 °C are given in Fig. S1. The E_g values of ZnO and Cu–ZnO

Table 3 Band gap energies of pure ZnO nanoparticles and Cu doped ZnO nanohybrids

	Band gap (eV)	
Sample	Sample calcined at 650 °C	Sample calcined at 450 °C
Pure ZnO	3.25	3.21
3% Cu–ZnO	3.20	3.10
5% Cu–ZnO	3.12	3.13
7% Cu–ZnO	3.09	3.03
10% Cu–ZnO	3.11	3.27

nanohybrids calcined at 450 °C and 650 °C are shown in Table 3. For the 450 °C samples, pure ZnO exhibited a band gap of 3.21 eV. With the introduction of Cu dopant, the band gap showed a non-monotonic trend, initially decreasing to a minimum of 3.03 eV at 7% Cu doping, followed by a slight increase to 3.27 eV at 10% doping. A similar trend was observed in the 650 °C samples, the band gap of pure ZnO was 3.25 eV, which reduced to 3.09 eV at 7% doping and increased slightly to 3.11 eV at 10% doping. The band gap of Cu-doped ZnO exhibits a non-monotonic behavior, initially decreasing at moderate doping levels and increasing again at higher concentrations. This is likely due to the formation of impurity energy levels and Cu^{2+} substitution at Zn^{2+} sites, which narrow the band gap via sp–d exchange interactions at lower doping levels. However, at higher dopant concentrations, factors such as the CuO phase segregation, and lattice distortion may contribute to band gap widening.[47,48]

When correlate with the AAS results, where among all Cu-doped ZnO nanoparticle samples, the 7% Cu-doped samples exhibited the highest actual Cu incorporation into the ZnO matrix. This enhanced incorporation directly influenced the electronic structure of ZnO, as evidenced by UV-vis DRS analysis, which showed that the 7% Cu–ZnO sample possessed the lowest band gap energy.

The observed narrowing of the band gap with increasing Cu content up to 7% is commonly attributed to the interaction between the host ZnO electronic states and the partially filled 3d orbitals of Cu^{2+} ions substituted into the ZnO lattice. These interactions modify the band structure via sp–d exchange interactions, leading to hybridization between Cu 3d states and the O 2p or Zn 4s orbitals, which causes a downward shift in the conduction band or an upward shift in the valence band, ultimately narrowing the band gap. This phenomenon has been reported in several studies on Cu-doped ZnO.[49–51]

As Cu^{2+} substitutes Zn^{2+} in the lattice, the creation of intermediate energy levels or the mixing of Cu 3d states with O 2p orbitals modifies the electronic structure, further contributing to the red shift (band gap narrowing) observed in Cu-doped ZnO. This incorporation disturbs the host crystal symmetry and introduces localized states near the conduction band, reducing the effective band gap.[44]

At a higher doping concentration of 10%, a slight increase in the band gap was observed, which can be attributed to the Burstein–Moss effect. This phenomenon occurs when an increased free electron concentration pushes the Fermi level into the conduction band, thereby blocking lower energy

transitions and resulting in an apparent widening of the band gap.[52–54]

The pronounced peak values in the Tauc plot (Fig. S1) for the 7% Cu-doped ZnO sample, where $(F(R) \cdot h\nu)^2$ is plotted as a function of photon energy, can be explained by the material's superior light absorption at this specific doping level. The incorporation of 7% Cu creates localized electronic states that enhance photon uptake in the UV-vis spectrum.[55,56] This effect causes a sharp reduction in diffuse reflectance (R), leading to an elevated Kubelka–Munk function value ($F(R)$), which is further intensified by the squaring operation in the Tauc plot.[57]

Comparatively, the 3% and 5% Cu-doped ZnO samples (Fig. S1) display much lower $F(R)$ values, likely a result of limited Cu integration and fewer defect sites, thus reducing their light absorbing capability. On the other hand, the 10% Cu-doped sample despite containing more copper—may suffer from dopant aggregation or clustering. This disrupts the ZnO crystal structure and diminishes efficient light absorption (Fig. S1). Accordingly, the higher $F(R)$ readings in the 7% Cu-doped ZnO highlight an optimal doping level for enhanced optical performance, while deviations in other concentrations lead to reduced absorbance due to structural and electronic factors.[58]

Scanning electron microscopy analysis further supported the XRD findings by revealing distinct morphological changes upon Cu doping. SEM analysis was conducted specifically for the samples with the lowest band gap energies at each temperature, 7% Cu–ZnO calcined at 450 °C and at 650 °C as well as for pure ZnO nanoparticles as a reference. The SEM images revealed that calcination temperature plays a crucial role in determining nanoparticle morphology (Fig. 2 and 3(c), (d)). At 450 °C, the nanoparticles displayed a relatively less aggregated and nanoflakes morphology, while the samples calcined at 650 °C exhibited more compact, spherical morphology, indicating enhanced crystallite growth. These morphological differences are attributed to the effect of temperature on nucleation and growth dynamics during calcination, where higher temperatures promote grain growth and densification, consistent with the reduction in surface defects and the observed narrowing of the band gap. This correlation between morphology and thermal treatment highlights the importance of temperature optimization in tailoring the physicochemical properties of Cu–ZnO nanomaterials for photocatalytic and antimicrobial applications. The SEM micrographs revealed that the shape and surface morphology of ZnO nanoparticles undergo noticeable changes upon Cu doping, even when the calcination temperature is held constant at 450 °C. For pure ZnO, the nanoparticles retained a relatively uniform appearance however, a significant morphological transformation was observed at 7% Cu doping, where the particles exhibited more irregular and aggregated structures.[59] This suggests that Cu incorporation, particularly has a pronounced impact on the growth pattern and surface characteristics of ZnO. Thus, the morphological variations seen at 7% Cu doping reflect the strong influence of dopant concentration on ZnO nanostructure, even under identical thermal treatment conditions.[60]

To evaluate the elemental composition of the synthesized nanoparticles, energy dispersive X-ray (EDX) spectroscopy and atomic absorption spectroscopy (AAS) were employed. EDX analysis revealed the surface-level elemental distribution which is in Fig. S2–S5. AAS was used to determine the overall metal content within the bulk of the samples. The AAS results for Cu-doped ZnO nanoparticles synthesized at 450 °C and 650 °C are summarized in Table 4, showing the actual molar ratios of Cu to Zn. In this study, the measured Cu : Zn atomic ratios were consistently lower than the nominal doping concentrations of 3%, 5%, 7%, and 10%, indicating incomplete incorporation of copper ions into the ZnO lattice during co-precipitation synthesis. This phenomenon is commonly observed in wet chemical methods, where dopant solubility limits, ionic radius mismatch, and kinetic factors restrict dopant incorporation efficiency. Specifically, at higher doping levels, dopant ions may segregate to grain boundaries or precipitate as secondary CuO phases rather than substituting into Zn sites, reducing effective doping within the crystal lattice.[61–63] Moreover, understanding the limits of dopant incorporation guides optimization of synthesis parameters to improve doping homogeneity and functional performance in Cu-doped ZnO nanomaterials.

3.2 Evaluation of the photocatalytic activity of the synthesized pure ZnO and Cu–ZnO nanoparticles

The photocatalytic efficiency of Cu-doped ZnO nanoparticles synthesized at 450 °C and 650 °C was evaluated by monitoring the degradation of methylene blue (MB) dye under sunlight and dark conditions. The photocatalytic activity was assessed by monitoring the gradual decrease in the characteristic absorption peak of MB over time using UV-vis spectroscopy. Using the eqn (3), the degradation efficiency was calculated as the percentage of dye degradation relative to the initial concentration.

$$\text{Degradation efficiency (\%)} = \frac{C_0 - C_t}{C_t} \times 100\% \qquad (3)$$

where, C_0 = initial concentration of MB dye (at time $t = 0$), C_t = concentration of MB dye at time t.

The photocatalytic degradation of methylene blue (MB) dye using ZnO is well documented and involves the generation of reactive oxygen species (ROS) upon light irradiation. Initially, MB molecules adsorb onto the surface of ZnO nanostructures. When ZnO is irradiated with light possessing energy equal to or greater than its band gap, electrons are excited from the valence band (VB) to the conduction band (CB), generating electron–hole pairs (excitons).[64,65]

Table 4 AAS results of % Cu in samples synthesized at 450 °C and 650 °C

Nominal % of Cu	Actual % of Cu incorporated in 450 °C samples	Actual % of Cu incorporated in 650 °C samples
3% Cu–ZnO	0.9%	1.85%
5% Cu–ZnO	1.6%	2.28%
7% Cu–ZnO	3.2%	4.02%
10% Cu–ZnO	2.9%	2.25%

The photogenerated electrons in the conduction band react with adsorbed molecular oxygen to produce superoxide anion radicals ($O_2^{-\bullet}$), while the holes in the valence band oxidize surface hydroxyl groups or water molecules to generate hydroxyl radicals ($^{\bullet}OH$).[65] These highly reactive species are responsible for initiating a series of oxidation reactions that break down MB dye molecules, leading to their decolorization and mineralization into non-toxic end products such as CO_2 and H_2O.[66] The efficiency of this photocatalytic degradation depends on the rate of generation and lifetime of the electron–hole pairs and ROS, which are influenced by the surface area, crystallinity, and electronic structure of the ZnO photocatalyst.[66]

The intensity of the characteristic absorption peak at 663 nm progressively decreased with increasing exposure time from 0 to 1 hour, indicating the gradual degradation of methylene blue (MB) dye (Fig. S13 and S14). This reduction in absorbance confirms the photocatalytic activity of the synthesized Cu-doped ZnO nanohybrids, where the visible-light-driven degradation of the dye is attributed to the generation of reactive oxygen species (ROS) that oxidize the dye molecules over time. Fig. 4 illustrates the photocatalytic degradation of methylene blue (MB) dye under sunlight and dark conditions for pure ZnO samples synthesized at 450 °C and 650 °C, and also for the 7% Cu-doped ZnO nanohybrids synthesized at 450 °C and 650 °C which are corresponding to the lowest measured band gap energy at each temperatures. After 1 hour of sunlight exposure, the pure ZnO samples showed moderate photocatalytic activity, achieving degradation efficiencies of
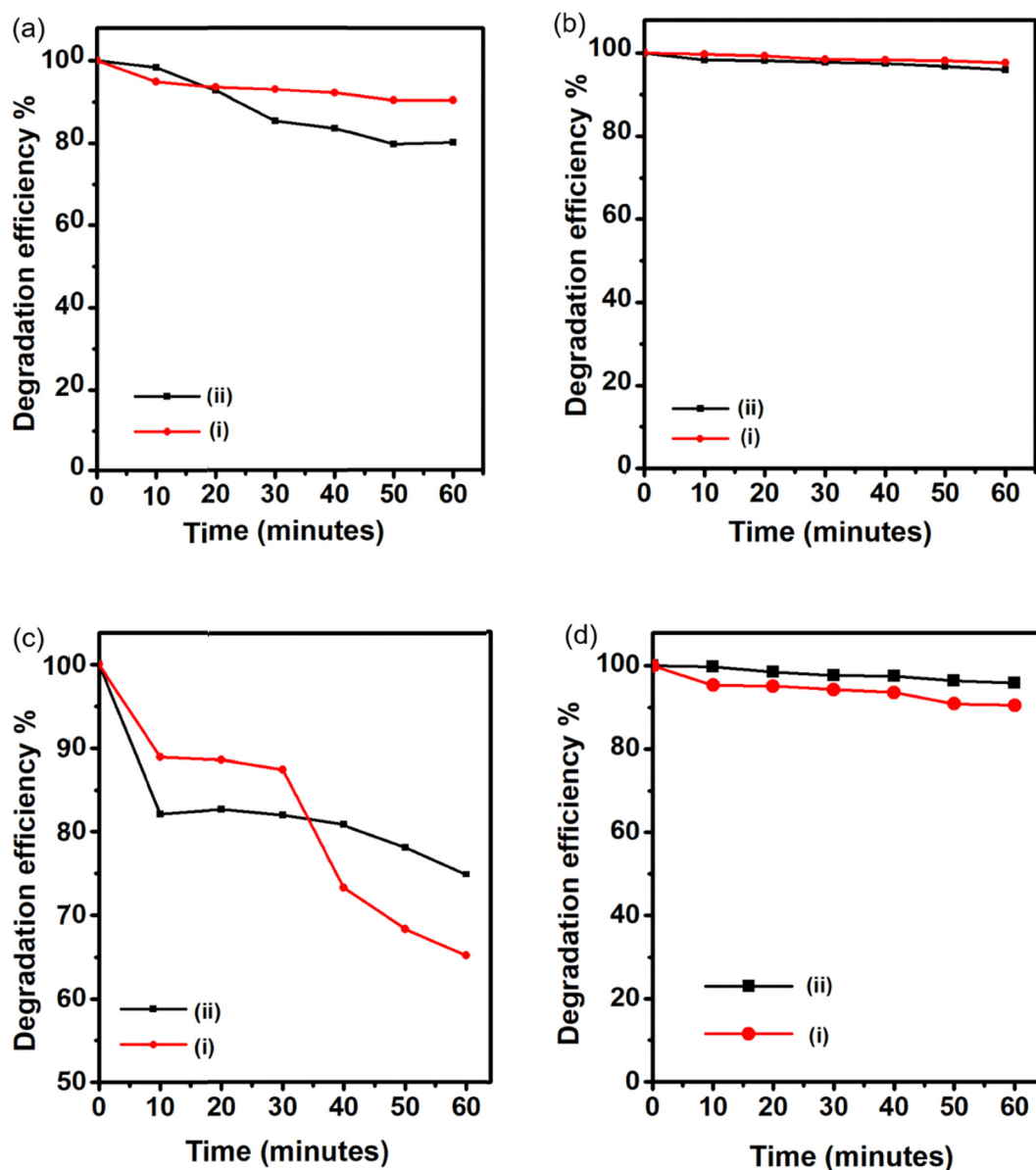

Fig. 4   Photocatalytic studies of (a) pure ZnO (i) 650 °C (ii) 450 °C under visible light; (b) pure ZnO (i) 650 °C (ii) 450 °C under dark; (c) 7% Cu–ZnO samples (i) 450 °C (ii) 650 °C under sunlight (intensity 45–75 Klux). (d) 7% Cu–ZnO samples (i) 450 °C (ii) 650 °C under dark.

Table 5 Photocatalytic degradation efficiency (%) of methylene blue over time under sunlight

Time (min)	ZnO (650 °C) (%)	ZnO (450 °C) (%)	7% Cu–ZnO (650 °C) (%)	7% Cu–ZnO (450 °C) (%)
10	5.14	1.70	17.91	11.07
20	6.47	7.36	17.33	11.38
30	7.06	14.67	17.99	12.59
40	7.91	16.48	19.11	26.74
50	9.67	20.51	21.78	31.68
60	9.74	20.02	25.03	34.77

20% and 10% for the 450 °C and 650 °C samples, respectively. In contrast, the 7% Cu-doped ZnO sample calcined at 450 °C demonstrated a significantly enhanced degradation efficiency of 35% within the same time period. The 7% Cu–ZnO sample prepared at 650 °C exhibited 25% degradation. The photocatalytic degradation efficiency (%) of methylene blue under sunlight over time for these samples is summarized in Table 5.

Under dark conditions, minimal dye degradation was observed in all samples, with values remaining below 5%, indicating that light irradiation is essential for the activation of photocatalytic processes of Cu–ZnO and ZnO semiconductor materials. Among the Cu-doped ZnO nanoparticles synthesized in this study, the 7% Cu–ZnO nanohybrids calcined at 450 °C exhibited the smallest average crystallite size, as confirmed by XRD analysis. The reduction in crystallite size results in a higher surface-to-volume ratio, which is a critical factor influencing photocatalytic activity.[67] An increased surface area enhances the adsorption of methylene blue (MB) molecules onto the photocatalyst surface, thereby facilitating improved interaction between the active sites and the target pollutant and ultimately boosting degradation efficiency.[68]

The photocatalytic degradation efficiencies of pure ZnO and Cu-doped ZnO nanoparticles synthesized in this study compare favorably with reported values in the literature, demonstrating the beneficial effect of Cu doping on photocatalytic performance. The 7% Cu–ZnO sample calcined at 450 °C exhibited a dye degradation efficiency of 35% under visible light within 60 minutes, which is notably higher than the 20% achieved by pure ZnO synthesized at the same temperature. This enhancement aligns well with previous reports where Cu doping in ZnO introduces intermediate energy levels and defect states that narrow the band gap, enabling visible-light activation and improved charge carrier separation. Differences in degradation efficiencies across studies can often arise from variations in synthesis methods, dopant concentrations, calcination temperatures, and particle morphologies; however, the positive trend in performance improvement with moderate Cu doping is consistently observed, confirming the effectiveness of the approach adopted in this work. The below Table 6 compares some previous studies with this work to further confirm the efficiency.[26]

3.3 Evaluation of IC$_{50}$ value of the synthesized pure ZnO (450 °C) and 7% Cu–ZnO (450 °C) by DPPH assay

To evaluate the antioxidant potential of the most active photocatalyst, the 7% Cu–ZnO nanohybrid synthesized at 450 °C was subjected to the DPPH (2,2-diphenyl-1-picrylhydrazyl) radical scavenging assay. This sample was selected due to its superior photocatalytic performance, lowest optical band gap energy (3.03 eV), and smallest crystallite size, which collectively indicate efficient charge transfer and enhanced surface reactivity. Pure ZnO synthesized at 450 °C was used as a control for comparative analysis. The DPPH assay is a widely accepted method for evaluating antioxidant activity by measuring free radical scavenging capacity.[74,75]

The IC$_{50}$ value represents the concentration at which 50% of the DPPH free radicals are effectively scavenged or neutralized. It is calculated using linear regression analysis by plotting the percentage of radical inhibition against the corresponding sample concentrations, as illustrated in Fig. 5. The IC$_{50}$ value of the control pure ZnO sample was found to be 441 μg mL^{-1}, whereas the 7% Cu-doped ZnO sample exhibited a significantly lower IC$_{50}$ value of 151 μg mL^{-1}, indicating a markedly higher radical scavenging activity.[76,77]

A closer examination of the DPPH assay data reveals a mechanism consistent with the well-established semiconductor-based photocatalysis principle. The free radical scavenging ability of the Cu–ZnO nanohybrids in methanolic DPPH solution can be attributed to the generation of reactive species upon bandgap excitation. Specifically, photoexcitation produces valence band holes (h$^+$) and conduction band electrons (e$^-$). The terminal hydroxyl (OH$^-$) groups on the nanohybrid surface facilitate the oxidation of water molecules to generate hydroxyl radicals ($^\bullet$OH), while the conduction band electrons react with molecular oxygen to form superoxide radicals (O$_2^{-\bullet}$), initiating a chain reaction that produces additional $^\bullet$OH radicals.[63,65]

These hydroxyl radicals, along with holes, interact with the DPPH molecules, accelerating the degradation of the purple-colored DPPH free radicals into a yellow, protonated, and stable form. This transformation aligns with the mechanism described by Kedare and Singh (2011), where the DPPH radical accepts electrons, stabilizing via conversion of unpaired electrons primarily located on nitrogen atoms, resulting in the observed color change.[78]

3.4 Evaluation of the antimicrobial activity of the nanohybrids
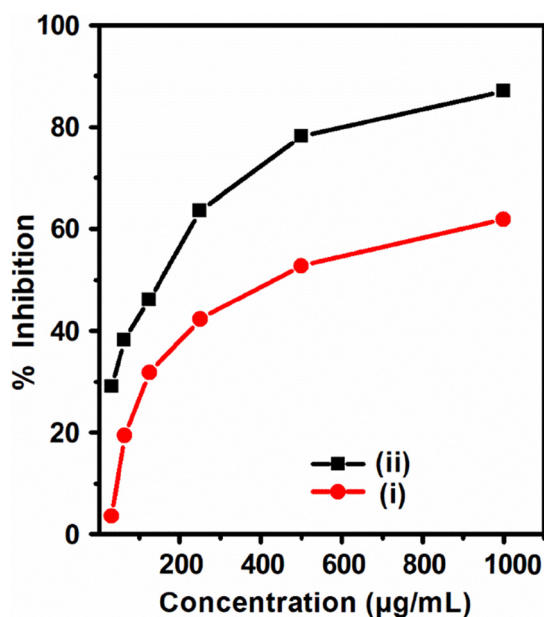
The antimicrobial efficacy of the synthesized 7% Cu-doped ZnO nanohybrid (450 °C) and pure ZnO (450 °C) was assessed using the agar well diffusion method against a spectrum of microbial strains, including both gram-positive (*Staphylococcus aureus* and MRSA) and gram-negative bacteria (*Escherichia coli*, *Salmonella typhi*, *Shigella sonnei*), as well as the fungus *Candida albicans*. The results revealed a clear enhancement in antimicrobial activity upon copper doping when compared to undoped ZnO nanoparticles. Notably, the 7% Cu-doped ZnO NPs calcined at 450 °C exhibited the highest antimicrobial efficacy across all tested strains, as shown in Fig. 6. The zone of inhibition (ZOI) data show that Cu–ZnO NPs generated significantly larger inhibition zones than pure ZnO NPs. For instance, the Cu–ZnO NPs produced ZOIs of 18.5 ± 0.5 mm for *S. aureus*, 15.83 ± 0.29 mm for MRSA, 25.5 ± 0.5 mm for *E. coli*,

Table 6 Comparison of photocatalytic degradation efficiencies (%) of pure ZnO and metal-doped ZnO samples for organic dye removal under different light conditions and durations, with corresponding literature references

Source	ZnO catalyst	Target dye (conc.)	Light source	Catalyst dose	Time (min)	Degradation
This study	**Pure ZnO (450 °C)**	**MB**	**Sunlight (45–75 klux)**	**20 mg**	**60**	**21%**
	7% Cu–ZnO (450 °C)	**MB**	**Sunlight (45–75 klux)**	**20 mg**	**60**	**35%**
Blažeka et al. 2022[69]	Pure ZnO	MB (2.7×10^{-5} M)	UV	~ 80 mg L^{-1}	60	$\sim 44\%$ ($\approx$)
	Ag (0.32%)–ZnO	MB (2.7×10^{-5} M)	UV	~ 80 mg L^{-1}	60	73%
Lins et al. 2023[70]	Ni (1%)–ZnO	MB (1.0×10^{-5} M)	UV (160 W)	500 mg L^{-1}	120	98.4%
Imboon et al. 2025[71]	Pure ZnO	RhB (10 mg L^{-1})	UV	—	1440	58%
	Fe–ZnO/GO	RhB (10 mg L^{-1})	UV	—	1440	99.3%
Chen et al. 2024[72]	Cu (0.5%)–ZnO	RhB	UV	—	120	$\sim 100\%$
Ranathunga et al.[73]	Pure ZnO	MB (4 mg L^{-1})	Sunlight (45–75 klux)	20 mg	60	27%
	Fe 5%–ZnO	MB (4 mg L^{-1})	Sunlight (45–75 klux)	20 mg	60	87%

Notes: MB = methylene blue; RhB = rhodamine B. For entries marked "$\approx$," values are approximate/derived from cited data. Catalyst doses not explicitly reported in some studies; "—" indicates not specified.

Fig. 5 DPPH free radical scavenging activity of (i) ZnO nanoparticles and (ii) 7% Cu–ZnO (450 °C).

27.33 ± 0.58 mm for *S. typhi*, 30.33 ± 0.58 mm for *S. sonnei*, and 31.67 ± 0.29 mm for *C. albicans*. In contrast, pure ZnO NPs under the same conditions only showed ZOIs of 13.33 ± 0.76 mm, 13.83 ± 0.29 mm, 17.66 ± 0.76 mm, 15.17 ± 0.76 mm, 15.83 ± 0.29 mm, and 15.17 ± 0.76 mm, respectively.

This enhanced antibacterial performance can be attributed to the synergistic effects of Cu incorporation into the ZnO lattice, which is known to increase the generation of reactive oxygen species (ROS), including hydroxyl radicals and superoxide anions. Through lipid peroxidation and the oxidation of organelles, such as proteins and DNA, reactive oxygen species (ROS), which are produced by radical scavenging activity, inhibit the antioxidant-dependent defense mechanism in microbial cells. The majority of bacteria create an acidic environment in their host cells, which causes catalysts to dissolve in biological fluids.[79] In this instance, the increasing acidity then promotes the production of hydroxyl groups.[80] As a

result, the bacterial cells will run out of glutathione and generate more ROS, which harm the microbial cells in a number of ways.[81] Collectively, these results validate the superior antibacterial and antifungal performance of 7% Cu–ZnO NPs and highlight the potential of Cu–Cu–ZnO-loaded nanofiber mats for biomedical and environmental antimicrobial applications.

In addition to ROS-mediated toxicity, copper doping also influences other physicochemical properties of ZnO nanoparticles that contribute to their enhanced antimicrobial efficacy. One such factor is the reduction in particle size and increase in surface area, which enhances nanoparticle–microbe interaction and facilitates greater ion release. The doped Cu^{2+} ions can also disrupt microbial cell membrane potential and interfere with ATP synthesis, further weakening cellular integrity. Moreover, Cu–ZnO nanoparticles have been reported to induce protein leakage and DNA fragmentation, particularly under oxidative stress conditions. The synergistic antibacterial activity is not only due to the combined effects of Zn^{2+} and Cu^{2+} ions but also their differential mechanisms of action, which help in minimizing the likelihood of microbial resistance development. Interestingly, the pronounced antifungal activity observed against *Candida albicans* indicates that Cu doping may alter surface charge distribution and hydrophobicity of the particles, improving adhesion to fungal membranes and increasing the internalization of particles into fungal cells.[82,83]

3.5 Characterization of the fabricated ZnO nanoparticles and 7% Cu–ZnO nanohybrid incorporated electrospun CA membranes

Based on the observed superior antibacterial and photocatalytic performance of 7% Cu-doped ZnO nanoparticles calcined at 450 °C, nanofiber membranes were fabricated by incorporating 7% Cu–ZnO nanohybrids (450 °C) and, as a control, pure ZnO (450 °C) into a cellulose acetate (CA) matrix *via* electrospinning. XRD analysis was carried out to investigate the structural characteristics of the resulting membranes. The XRD pattern of the CA incorporated with ZnO nanofibers displayed a broad diffraction peak, characteristic of the amorphous nature of cellulose acetate. And also, for ZnO nanofiber membrane and Cu-doped ZnO nanofiber membrane, additional sharp
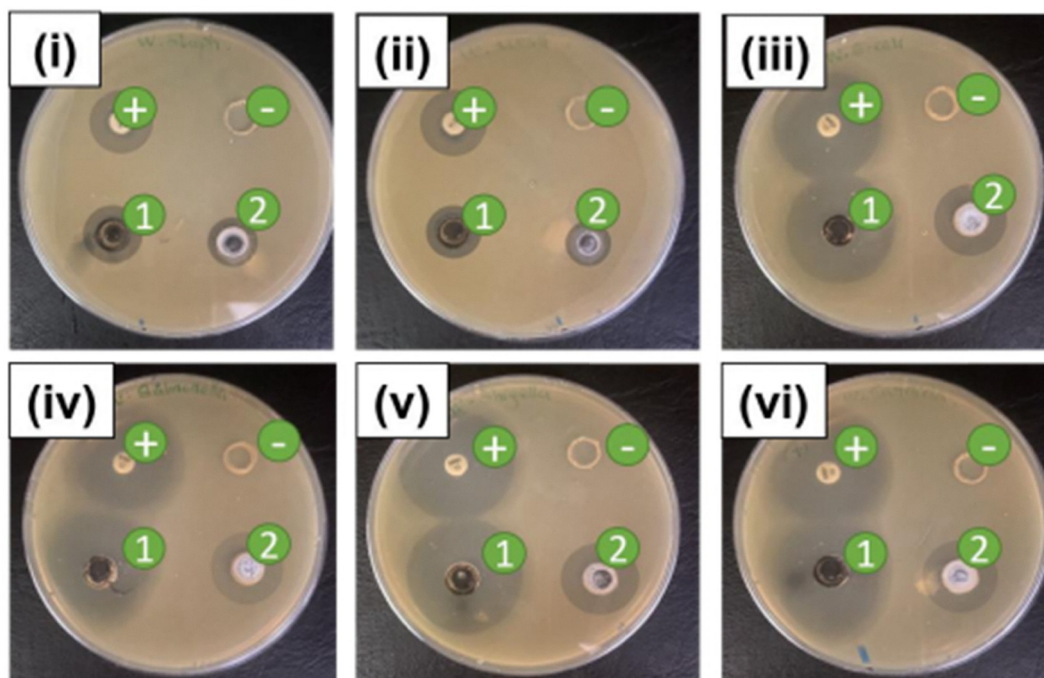
Fig. 6 (i) *S. aureus*, (ii) MRSA, (iii) *E. coli*, (iv) *Salmonella typhi*, (v) *Shigella sonnei*, (vi) *C.* albicans; (+) positive control, (−) negative control, (1) 7% Cu doped ZnO and (2) ZnO (each well contains 50 µL of 100 mg L^{-1} dispersion).

diffraction peaks appeared in the 2θ range of 20°–80° of Fig. 7(a), corresponding to the hexagonal wurtzite structure of ZnO. For the Cu 7%–ZnO nanohybrid-loaded CA mats, prominent diffraction peaks were indexed to the (100), (002), (101), (102), (110), (103), (112), and (201) planes, confirming the presence of crystalline ZnO. The absence of secondary or impurity phases in all samples suggests high phase purity and successful incorporation of the doped nanostructures within the polymer matrix.

Complementing the XRD findings, FTIR analysis further confirmed the successful incorporation of nanohybrids within the cellulose acetate (CA) matrix for both pure ZnO/CA and 7% Cu–ZnO/CA electrospun mats. The FTIR spectra (Fig. 7(b)) of both fiber mats exhibit characteristic absorption bands of CA around 1730 cm^{-1} (C=O stretching of acetyl groups), around 1360 cm^{-1} (C–H bending), around 1240 cm^{-1} (C–O stretching in ester), and around 1024 cm^{-1} (C–O–C asymmetric stretching), which are consistent with previously reported CA structure.[84,85] These peaks confirm that the polymer backbone remains intact during electrospinning and nanohybrid loading. In addition to the polymer-specific peaks, distinctive metal–oxygen vibrational bands were observed in the low wavenumber region, indicating the successful incorporation of metal oxides. Specifically, the ZnO/CA mat exhibits a characteristic Zn–O stretching vibration around 647 cm^{-1}, whereas in the Cu-doped ZnO/CA mat, a Cu–O stretching vibration appears near 529 cm^{-1}. Additionally, both mats show bands in the region of 890–910 cm^{-1}, which can be attributed to peroxide (M–O–O–M) formation, consistent with metal–oxygen–oxygen–metal bonding vibrations observed in similar metal oxide systems.

To analyze the chemical composition of nanofiber membranes, AAS was carried out for electrospun mats. About 1 cm × 1 cm

(1 cm^2) of pieces were collected from the five different places on the mats and analyzed the composition of Zn and Cu metals. As illustrated on Fig. 7(e), the composition of Zn, throughout the ZnO electrospun mat was homogeneous. This was confirmed statistically by the ANOVA test. And the results are included in Fig. S8 and S9. When consider about the Cu–ZnO mat, it also confirmed the homogeneous distribution of Zn throughout the mat. The amount of Cu loaded to the nanoparticles was very small. And the amount used to electrospun could be much smaller. But to check the homogeneity statistically, the two sample *t* test was conducted. The results included in Fig. S10, and it also confirmed the homogeneous distribution of Cu metal. Homogeneous distribution is important to increase the efficiency of photocatalytic degradation. And also, it confirms the most suitable electrospinning parameters were used to fabricate the mats using CA.

The morphology of electrospun cellulose acetate (CA) nanofibers incorporating ZnO and 7% Cu–ZnO NPs calcined at 450 °C was examined using scanning electron microscopy (SEM), as shown in Fig. 7(c) and (d). In both ZnO–CA and Cu–ZnO–CA nanofiber membranes, the presence of beads along the fibers was observed, which is typically considered a defect in electrospun materials. However, incorporation of nanoparticles clearly influenced the fiber morphology. A notable reduction in fiber diameter was observed upon doping ZnO with 7% Cu. This reduction in diameter can be attributed to the increased charge density on the electrospinning jet due to the presence of Cu-doped ZnO nanoparticles. As the charge on the jet increases, the electrostatic repulsion within the jet is more effectively counteracted by elongational forces under the electric field, leading to the formation of finer fibers. SEM micrographs were analyzed using ImageJ software to quantify fiber diameters and assess their
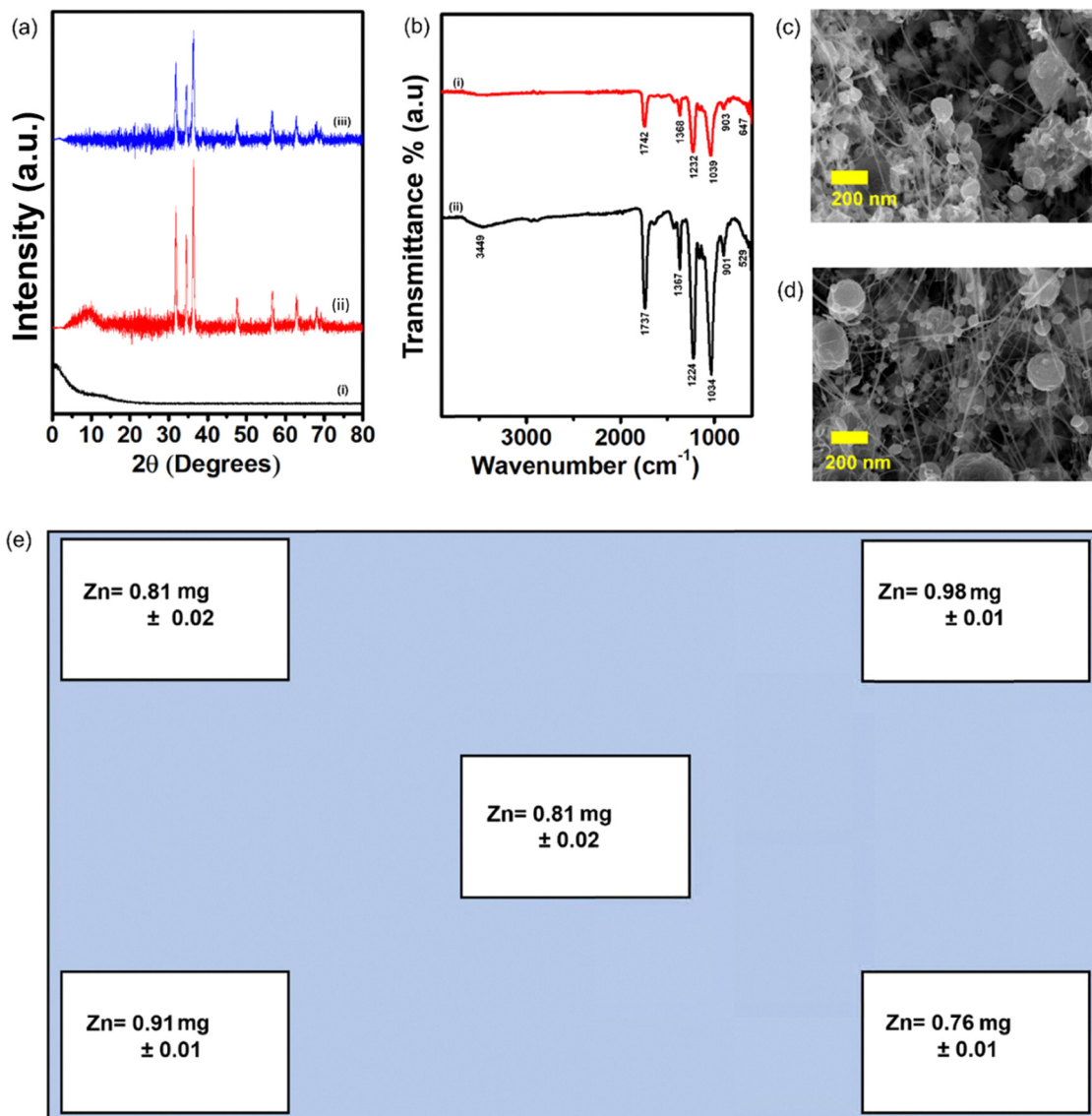
Fig. 7 (a) PXRD spectra of (i) CA mat (ii). Pure ZnO/CA (iii). 7% Cu–ZnO/CA and (b) FTIR analysis of nanofiber membranes of (i). Pure ZnO/CA (ii). 7% Cu–ZnO/CA, (c) SEM image of ZnO 450 °C CA nanofiber membrane (d) SEM image of 7% Cu–ZnO 450 °C CA nanofiber membrane (e) Zn metal distribution throughout the nanofiber membrane with 7% Cu–ZnO/CA.

distribution. The average fiber diameter for the pure ZnO nanofibers was 6.236 ± 0.299 nm, while the 7% Cu–ZnO nanofibers exhibited a slightly reduced mean diameter of 5.607 ± 0.108 nm. This observation supports the hypothesis that metal doping can significantly influence jet dynamics during electrospinning, resulting in finer and more uniformly distributed fibers.[86] The histogram distribution of size of the nanofibers shows in the Fig. S11. Additionally EDX analysis was performed along with the SEM, which are shown in Fig. S6 and S7.

3.6 Evaluation of the photocatalytic activity of pure ZnO and 7% Cu–ZnO nanohybrid incorporated CA electrospun nanofiber membranes

The photocatalytic performance of the electrospun fiber mats embedded with pure ZnO and 7% Cu-doped ZnO nanohybrids synthesized at 450 °C was assessed by monitoring the degradation of methylene blue (MB) dye over a 60 minute period (Fig. S15). As shown in the Fig. 8; the 7% Cu–ZnO incorporated fiber mat achieved a degradation efficiency of 30%, while the pure ZnO fiber mat displayed a comparatively lower degradation efficiency of 18%. This enhancement in degradation capacity upon Cu doping suggests improved photocatalytic activity due to the presence of Cu ions, which can act as electron traps, reducing the recombination rate of photogenerated electron–hole pairs. When compared to the degradation performance of the corresponding nanoparticles the 7% Cu–ZnO nanoparticles exhibited 35% MB degradation, whereas the pure ZnO nanoparticles showed 20% degradation under the same conditions. Although the nanoparticle forms demonstrated slightly higher activity than their respective nanofiber composites, the performance gap was not significant. In fact, the nanofiber membranes offer advantages in terms of mobilization, material handling, recovery, and
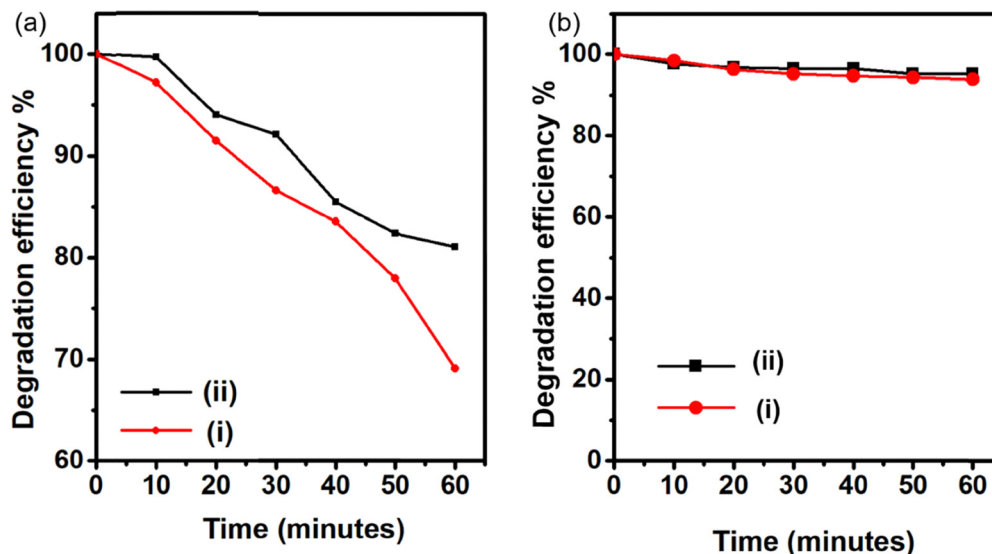
Fig. 8 Photocatalytic studies of nanofiber membranes (a) under visible light (i) 7% Cu−ZnO/CA (ii) pure ZnO/CA (b) under dark (i) 7% Cu−ZnO/CA (ii) pure ZnO/CA.

recyclability, making these mats promising candidates for real world applications.[87]

3.7 Evaluation of radical scavenging activity of ZnO nanoparticles and 7% Cu–ZnO nanohybrid incorporated electrospun CA membranes by DPPH assay

Rate based kinetic studies offer a dynamic understanding of how quickly the radical scavenging reaction progresses over time. By modeling the temporal evolution of DPPH decolorization, rate calculations reveal not just the extent, but also the speed and mechanism of radical neutralization. This becomes particularly important when comparing materials with similar IC_{50} values, as a faster reaction rate can indicate superior kinetics and enhanced surface reactivity.[88,89]

In our study, the DPPH radical scavenging activity of pure ZnO and 7% Cu-doped ZnO nanofiber mats were evaluated over time and fitted to three kinetic models: zeroth-order, pseudo-first order, and pseudo-second order. From above Fig. 9(a)–(c), the zeroth-order model yielded the highest correlation coefficients (R^2 = 0.9951 for 7% Cu–ZnO and 0.9515 for ZnO), which indicated in the Table 7, that the reaction follows a concentration independent rate where the radical scavenging is primarily governed by the availability of active sites and reactive surface electrons.

The poor linear regression coefficients (R^2 values) for the CA mat in all kinetic models indicate that the cellulose acetate (CA) mat itself exhibits very limited or negligible free radical scavenging activity. This is expected because CA is an inert polymer lacking active sites or functional groups capable of donating electrons or hydrogen atoms that are necessary to neutralize free radicals.[90] Thus, the scavenging reaction in the CA mat does not follow these kinetic models well, resulting in poor fits. The zero-order model shows the best linear regression coefficient for the pure ZnO/CA mat and 7% Cu–ZnO/CA mat, which

suggests that the radical scavenging activity by these materials proceeds at a relatively constant rate independent of the concentration of free radicals. This behavior points to a reaction limited mostly by the availability of active sites on the ZnO or Cu-doped ZnO surfaces rather than by the concentration of DPPH radicals in solution.[26]

This enhancement can be attributed to the presence of Cu^{2+} ions, which introduce defect states and increase the charge carrier density, thereby facilitating more efficient electron transfer to the DPPH radicals. Furthermore, the improved rate is consistent with the higher photocatalytic activity observed in methylene blue degradation experiments for the same nanofiber composition. Both processes rely on redox activity, and the faster radical scavenging rate confirms the increased surface reactivity and electron availability of the Cu-doped ZnO system.[56] Therefore, kinetic rate analysis not only complements IC_{50} data but also provides a more nuanced understanding of the material's reactivity, especially for applications involving real-time antioxidant or photocatalytic functions. About 2 hours time period however, the scavenging activity reached a plateau beyond approximately 80 minutes, with only negligible changes observed thereafter. The 7% Cu–ZnO/CA mat had the highest radical scavenging activity (around 80%) after 80 minutes as shown in Fig. 9(d).

3.8 Evaluation of antimicrobial activity of ZnO nanoparticles and 7% Cu–ZnO nanohybrid incorporated electrospun CA membranes by disc diffusion method

The antimicrobial efficacy of electrospun nanofiber membranes embedded with 7% Cu-doped ZnO nanohybrids (450 °C) and pure ZnO (450 °C) was systematically investigated using the disc diffusion method against pathogenic microorganisms, which were also tested against 7% Cu–ZnO nanohybrids previously. Strains included gram-positive bacteria
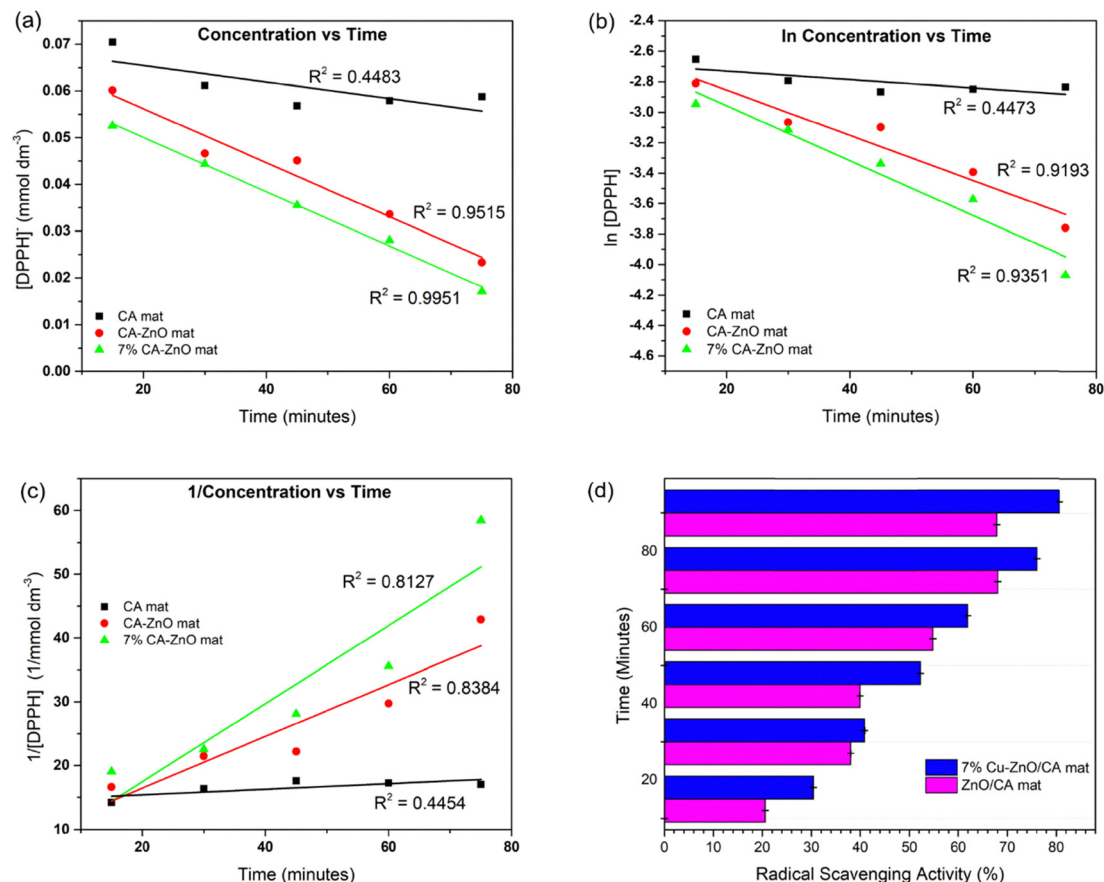
Fig. 9 The kinetic order plots (a) zeroth order (b) pseudo-first order (c) pseudo-second order, for CA mat, pure ZnO/CA and 7% Cu–ZnO/CA nanofiber mats (d) % RSA of ZnO/CA and 7% Cu–ZnO/CA nanofiber mats at different time intervals.

(*Staphylococcus aureus* and MRSA), gram-negative bacteria (*Escherichia coli*, *Salmonella typhi*, *Shigella sonnei*), and the fungus *Candida albicans*. Consistent with the nanoparticle results, the incorporation of copper significantly enhanced the antimicrobial performance of the nanofiber mats. As shown in Fig. 10, the 7% Cu–ZnO nanofiber mats exhibited markedly larger zones of inhibition (ZOIs) across all tested strains compared to mats containing pure ZnO nanoparticles. Specifically, the 7% Cu–ZnO mats produced ZOIs of 17.66 ± 0.76 mm for *S. aureus*, 16.33 ± 0.29 mm for MRSA, 25.5 ± 0.5 mm for *E. coli*, 29.17 ± 0.29 mm for *S. typhi*, 28.17 ± 0.28 mm for *S. sonnei*, and 31.17 ± 0.29 mm for *C. albicans*. In contrast, the pure ZnO nanofiber mats showed significantly lower inhibition zones of 13.33 ± 0.58 mm, 14.33 ± 0.28 mm, 17.66 ± 0.76 mm, 18.16 ± 0.29 mm, 16.33 ± 0.29 mm, and 17.17 ± 0.29 mm, respectively.[91]

The enhanced antimicrobial efficacy observed with the 7% Cu–ZnO nanofiber membranes can be scientifically attributed to the multifaceted role of copper as a functional dopant within the ZnO matrix. Copper doping introduces lattice distortions and oxygen vacancies, which facilitate a higher generation of reactive oxygen species (ROS); including hydroxyl radicals, superoxide anions, and hydrogen peroxide. These ROS are particularly effective at inducing oxidative stress in microbial cells, damaging vital cellular components such as lipids, proteins, and nucleic acids. The action mechanism varies slightly depending on the type of microorganism. In gram-negative bacteria like *Escherichia coli*, *Salmonella typhi*, and *Shigella sonnei*, the outer membrane contains lipopolysaccharides that are susceptible to ROS and metal ion-induced disruption, allowing deeper penetration of toxic species into the

Table 7 The k (rate constant) values and R^2 values of zeroth order, pseudo-first order and pseudo-second-order kinetic graphs for CA mat, pure ZnO/CA and 7% Cu–ZnO/CA mats

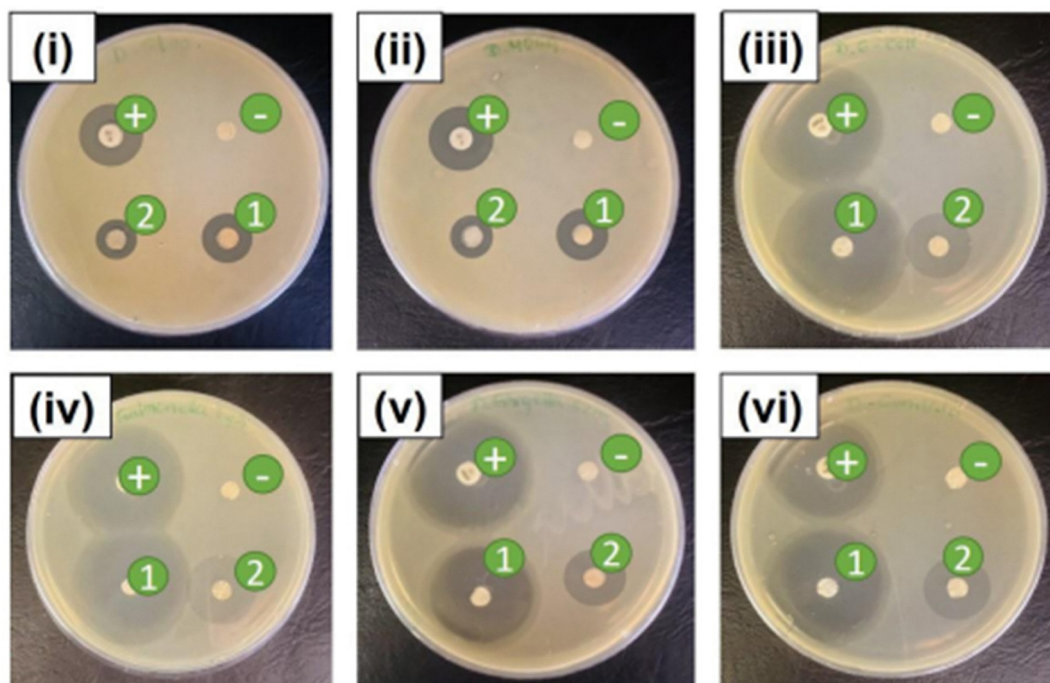| Sample	Zeroth order		Pseudo-first order		Pseudo-second order	
	R^2	k value (mM min^{-1})	R^2	k value (min^{-1})	R^2	k value (mM^{-1} min^{-1})
CA mat	0.4483	-1.77619×10^{-4}	0.4473	-0.00278	0.4454	0.04378
Pure ZnO/CA mat	0.9515	-5.77989×10^{-4}	0.9193	-0.01482	0.8384	0.40585
7% Cu–ZnO/CA mat	0.9951	-5.80947×10^{-4}	0.9351	-0.01801	0.8127	0.61268

Fig. 10 (i) *S. aureus*, (ii) MRSA, (iii) *E. coli*, (iv) *Salmonella typhi*, (v) *Shigella sonnei*, (vi) *C. albicans*; (+) positive control, (−) negative control, (1) 7% Cu doped ZnO, and (2) ZnO (loading = 40% w/w).

periplasmic space and cytoplasm. This likely contributes to the more pronounced inhibition zones observed for these strains. In contrast, gram-positive bacteria such as *Staphylococcus aureus* and MRSA possess a thicker peptidoglycan layer, which can partially shield internal components from oxidative damage; however, Cu^{2+} ions can still penetrate and interfere with intracellular enzyme systems and DNA replication processes. The antifungal action against *Candida albicans* appears even more pronounced, which may be due to the unique interaction of Cu–ZnO with fungal cell walls composed of chitin and β-glucans, as well as the induction of mitochondrial dysfunction by ROS. Furthermore, the electrospun nanofiber architecture enhances these effects by providing a high surface area for microbial contact, promoting sustained ion release and close-range ROS activity.[92,93]

As a comparison, Table 8 presents the antimicrobial performance of ZnO nanoparticles, 7% Cu-doped ZnO nanoparticles, ZnO/CA nanofiber mats, and 7% Cu–ZnO/CA nanofiber mats. The results clearly demonstrate that both the 7% Cu-doped ZnO nanoparticles and their corresponding nanofiber mats

exhibit pronounced antimicrobial activity against all tested pathogens. In most cases, the zones of inhibition (ZOI) observed for the nanohybrids and the nanofiber mats are highly comparable, with only minor variations. These findings indicate that the incorporation of the nanohybrids into electrospun CA nanofiber mats does not significantly diminish their antimicrobial efficacy, as the active agents remain effective despite being immobilized within the mat. Moreover, the 7% Cu–ZnO nanofiber mats retain the strong antimicrobial performance of the free nanohybrids while providing additional benefits such as improved stability, controlled release, and enhanced potential for advanced antimicrobial applications.

4. Conclusion

In the present work, ZnO and Cu-doped ZnO nanohybrids were successfully synthesized using the co-precipitation method, followed by calcination at 450 °C and 650 °C. Various Cu doping concentrations (3%, 5%, 7%, and 10%) were investigated

Table 8 Antimicrobial activity of ZnO and 7% Cu−ZnO nanohybrids and their nanofiber mats in mm

Microorganism	Pure ZnO nanoparticles (450 °C)	7% Cu–ZnO nanoparticles (450 °C)	Pure ZnO nanofiber Mat (450 °C)	7% Cu–ZnO nanofiber Mat (450 °C)
Staphylococcus aureus	13.33 ± 0.76	18.5 ± 0.50	13.33 ± 0.58	17.66 ± 0.76
MRSA	13.83 ± 0.29	15.83 ± 0.29	14.33 ± 0.28	16.33 ± 0.29
Escherichia coli	17.66 ± 0.76	25.5 ± 0.50	17.66 ± 0.76	25.5 ± 0.50
Salmonella typhi	15.17 ± 0.76	27.33 ± 0.58	18.16 ± 0.29	29.17 ± 0.29
Shigella sonnei	15.83 ± 0.29	30.33 ± 0.58	16.33 ± 0.29	28.17 ± 0.28
Candida albicans	15.17 ± 0.76	31.67 ± 0.29	17.17 ± 0.29	31.17 ± 0.29

to study their effects on structural, optical, antioxidant, and antimicrobial properties of ZnO. PXRD analysis revealed that all samples maintained the hexagonal wurtzite structure of ZnO without detectable impurity phases, and the crystallite size was influenced by both doping level and calcination temperature. Among all synthesized samples, the 7% Cu-doped ZnO nanohybrid calcined at 450 °C demonstrated the most balanced and superior performance. Optical measurements showed a red-shift in band gap energy upon Cu doping, suggesting improved visible light absorption. DPPH radical scavenging assay confirmed enhanced antioxidant activity for the 7% Cu–ZnO 450 °C sample compared to pure ZnO. Photocatalytic degradation of methylene blue under normal light demonstrated that 7% Cu–ZnO nanoparticles achieved a degradation efficiency of 35% within 60 minutes, significantly outperforming undoped ZnO (20%). This enhanced activity was retained even after electrospinning into cellulose acetate nanofibers, with the 7% Cu–ZnO mat achieving 30% degradation indicating excellent compatibility and functional integration within the polymer matrix. Antimicrobial studies using the agar well diffusion method showed that the 7% Cu–ZnO nanohybrids had significantly larger zones of inhibition (ZOIs) across all tested pathogens, including *Staphylococcus aureus*, MRSA, *Escherichia coli*, *Salmonella typhi*, *Shigella sonnei*, and *Candida albicans*, when compared to pure ZnO. The electrospun nanofiber mats also exhibited strong antimicrobial efficacy, with ZOIs closely comparable to their nanoparticle counterparts, highlighting their potential for practical applications in biomedical fields. Altogether, the 7% Cu–ZnO nanohybrid synthesized at 450 °C exhibited optimized structural and functional performance and was chosen for nanofiber fabrication. The resulting Cu–ZnO nanofiber mats offer a robust platform combining photocatalytic, antioxidant, and antimicrobial functionalities, suggesting their promising application as photocatalytic and advanced antimicrobial technologies.

Author contributions

Hasitha Herath – conduct the experiment, formal analysis of data and writing the manuscript. Pasindu Viduranga – conduct the experiment, formal analysis of data and writing the manuscript. Piumika Yapa – conduct microbiology experiments, formal analysis of data and writing the manuscript. Sanduni Dabare – conduct the experiment, formal analysis of data and writing the manuscript. Imalka Munaweera – conceptualization, funding acquisition, methodology, supervision, writing, review and editing the original draft. Manjula M. Weerasekera – supervision and curation of microbiology data, review and editing the original draft. Upeka Samarakoon – supervision and curation of PXRD characterization data, review and editing the original draft. All authors have approved the final version of the manuscript.

Conflicts of interest

There are no conflicts of interest to declare.

Data availability

All data produced and analyzed in this research are included in this manuscript.

Acknowledgements

References

1 T. Su and X. Zhu, Advanced Photocatalytic Materials for Environmental and Energy Applications, *Materials*, 2023, **16**(22), 7197. Available from: **https://www.mdpi.com/1996-1944/16/22/7197**.

2 K. Chen, W. Dong, Y. Huang, F. Wang, J. L. Zhou and W. Li, Photocatalysis for sustainable energy and environmental protection in construction: A review on surface engineering and emerging synthesis, *J. Environ. Chem. Eng.*, 2025, **13**(5), 117529. Available from: **https://www.sciencedirect.com/science/article/pii/S2213343725022250**.

3 M. A. Hassaan, M. A. El-Nemr, M. R. Elkatory, S. Ragab, V. C. Niculescu and A. El Nemr, Principles of Photocatalysts and Their Different Applications: A Review, *Top. Curr. Chem.*, 2023, **381**(6), 31, DOI: **10.1007/s41061-023-00444-7**.

4 S. He, Y. Chen, J. Fang, Y. Liu and Z. Lin, Optimizing photocatalysis via electron spin control, *Chem. Soc. Rev.*, 2025, **54**(5), 2154–2187, DOI: **10.1039/D4CS00317A**.

5 A. Kumar, S. Rana, P. Dhiman, C. W. Lai, G. Sharma and T. Wang, Advances in enhancing the photocatalytic potential of AgVO3 catalyst for environmental and energy applications: A review, *J. Environ. Chem. Eng.*, 2025, **13**(4), 117276. Available from: **https://www.sciencedirect.com/science/article/pii/S2213343725019724**.

6 S. Ma, Y. Huang, R. Hong, X. Lu, J. Li and Y. Zheng, Enhancing Photocatalytic Activity of ZnO Nanoparticles in a Circulating Fluidized Bed with Plasma Jets, *Catalysts*, 2021, **11**(1), 77. Available from: **https://www.mdpi.com/2073-4344/11/1/77**.

7 J. Khumphon, R. Ahmed, T. Imboon, J. Giri, N. Chattham and F. Mohammad, *et al.*, Boosting Photocatalytic Activity in Rhodamine B Degradation Using Cu-Doped ZnO Nanoflakes, *ACS Omega*, 2025, **10**(9), 9337–9350, DOI: **10.1021/acsomega.4c10034**.

8 I. A. Hassan, S. Sathasivam, S. P. Nair and C. J. Carmalt, Antimicrobial Properties of Copper-Doped ZnO Coatings under Darkness and White Light Illumination, *ACS Omega*, 2017, **2**(8), 4556–4562, DOI: **10.1021/acsomega.7b00759**.

9 S. Meghana, P. Kabra, S. Chakraborty and N. Padmavathy, Understanding the pathway of antibacterial activity of copper oxide nanoparticles, *RSC Adv.*, 2015, **5**(16), 12293–12299, DOI: **10.1039/C4RA12163E**.

10 S. Arooj, S. Nazir, A. Nadhman, N. Ahmad, B. Muhammad and I. Ahmad, *et al.*, Novel ZnO:Ag nanocomposites induce significant oxidative stress in human fibroblast malignant melanoma (Ht144) cells, *Beilstein J. Nanotechnol.*, 2015, **6**, 570–582, DOI: **10.3762/bjnano.6.59**.

11 C. Voorhis, J. González-Benito and A. Kramar, "Nano in Nano"—Incorporation of ZnO Nanoparticles into Cellulose Acetate–Poly(Ethylene Oxide) Composite Nanofibers Using Solution Blow Spinning, *Polymers*, 2024, **16**(3), 341. Available from: **https://www.mdpi.com/2073-4360/16/3/341**.

12 R. Chen, S. M. Tian, J. Song, G. T. Zhao, X. Cao, Q. Y. Shi, *et al.*, *Preparation of Zinc oxide nanofibers and their photocatalytic degradation and antibacterial properties*, 2025.

13 K. Ranathunga, P. Yapa, I. Munaweera, M. M. Weerasekera and C. Sandaruwan, Preparation and characterization of Fe–ZnO cellulose-based nanofiber mats with self-sterilizing photocatalytic activity to enhance antibacterial applications under visible light, *RSC Adv.*, 2024, **14**(26), 18536–18552, DOI: **10.1039/D4RA03136A**.

14 P. L. Nguyen, T. N. Tran, M. T. Le, A. Ullah, D. N. Phan and I. S. Kim, Enhanced Dye Removal and Antibacterial Efficacy of Copper-Doped ZnO Nanoparticles on Cellulose Nanofibers, *Adv. Mater. Interfaces*, 2024, **11**(35), 2400468. Available from: **https://advanced.onlinelibrary.wiley.com/doi/abs/10.1002/admi.202400468**.

15 P. Yapa, I. Munaweera, M. M. Weerasekera and L. Weerasinghe, Synergistic antimicrobial nanofiber membranes based on metal incorporated silica nanoparticles as advanced antimicrobial layers, *RSC Adv.*, 2024, **14**(46), 33919–33940, DOI: **10.1039/D4RA05052E**.

16 J. Qin, X. Zhang, C. Yang, M. Cao, M. Ma and R. Liu, ZnO microspheres-reduced graphene oxide nanocomposite for photocatalytic degradation of methylene blue dye, *Appl. Surf. Sci.*, 2017, **392**, 196–203. Available from: **https://www.sciencedirect.com/science/article/pii/S0169433216319110**.

17 I. P. Madhushika, P. Yapa, I. Munaweera, C. Sandaruwan and M. M. Weerasekera, The antimicrobial synergy of polymer based nanofiber mats reinforced with antioxidants intercalated layered double hydroxides as a potential active packaging material, *Nano Express*, 2024, **5**(2), 25018, DOI: **10.1088/2632-959X/ad4a95**.

18 U. Alver, T. Kılınç, E. Bacaksız and S. Nezir, Structure and optical properties of Zn1−xFexO thin films prepared by ultrasonic spray pyrolysis, *Mater. Sci. Eng., B*, 2007, **138**(1), 74–77. Available from: **https://www.sciencedirect.com/science/article/pii/S0921510707000323**.

19 K. T. Kim, G. H. Kim, J. C. Woo and C. I. Kim, Characteristics of Nickel-doped Zinc Oxide thin films prepared by sol–gel method, *Surf. Coat. Technol.*, 2008, **202**(22), 5650–5653. Available from: **https://www.sciencedirect.com/science/article/pii/S0257897208005252**.

20 P. Jongnavakit, P. Amornpitoksuk, S. Suwanboon and N. Ndiege, Preparation and photocatalytic activity of Cu-doped ZnO thin films prepared by the sol–gel method, *Appl. Surf. Sci.*, 2012, **258**(20), 8192–8198. Available from: **https://www.sciencedirect.com/science/article/pii/S0169433212008665**.

21 P. Raju, D. Deivatamil, J. A. Martin Mark and J. P. Jesuraj, Antibacterial and catalytic activity of Cu doped ZnO nanoparticles: structural, optical, and morphological study, *J. Iran. Chem. Soc.*, 2022, **19**(3), 861–872, DOI: **10.1007/s13738-021-02352-3**.

22 G. S. Rohrer, "Introduction to Grains, Phases, and Interfaces—an Interpretation of Microstructure," Trans. AIME, 1948, vol. 175, pp. 15–51, by C.S. Smith, *Metall. Mater. Trans. A*, 2010, **41**(5), 1063–1100, DOI: **10.1007/s11661-010-0215-5**.

23 A. Rollett, F. Humphreys and G. S. Rohrer, Hatherly M. Recrystallization and Related Annealing Phenomena, *Recrystallization and Related Annealing Phenomena*, 2nd edn, 2004, pp. 1–628.

24 A. Mahmoud, M. Echabaane, K. Omri, J. Boudon, L. Saviot and N. Millot, *et al.*, Cu-Doped ZnO Nanoparticles for Non-Enzymatic Glucose Sensing, *Molecules*, 2021, **26**(4), 929. Available from: **https://www.mdpi.com/1420-3049/26/4/929**.

25 S. Sivakumar, Y. Robinson and N. A. Mala, Studies on photocatalytic performance and supercapacitor applications of undoped and Cu-doped ZnO nanoparticles, *Appl. Surf. Sci. Adv.*, 2022, **12**, 100344. Available from: **https://www.sciencedirect.com/science/article/pii/S2666523922001349**.

26 V. Pasindu, P. Yapa, S. Dabare, I. Munaweera, T. Etampawala and M. M. Weerasekera, *et al.*, Harnessing the power of visible light with GO-Ni-ZnO nanohybrid electrospun polymeric membranes for improved photocatalysis: a focused approach to fabrication, characterization, and applications, *Emergent Mater.*, 2025, 1–26, DOI: **10.1007/s42247-025-01188-4**.

27 A. R. West, *Solid State Chemistry and its Applications*, John Wiley & Sons, 2022.

28 Ü. Özgür, Y. A. I. Alivov, C. Liu, A. Teke, M. A. Reshchikov and S. Doğan, *et al.*, A comprehensive review of ZnO materials and devices, *J. Appl. Phys.*, 2005, **98**(4), 041301, DOI: **10.1063/1.1992666**.

29 D. Dasuki, K. Habanjar and R. Awad, Effect of Growth and Calcination Temperatures on the Optical Properties of Ruthenium-Doped ZnO Nanoparticles, *Condens. Matter*, 2023, **8**(4), 102. Available from: **https://www.mdpi.com/2410-3896/8/4/102**.

30 S. Singhal, J. Kaur, T. Namgyal and R. Sharma, Cu-doped ZnO nanoparticles: Synthesis, structural and electrical properties, *Phys. B*, 2012, **407**(8), 1223–1226. Available from: **https://www.sciencedirect.com/science/article/pii/S0921452612001196**.

31 A. Shahpal, M. A. Choudhary and Z. Ahmad, An investigation on the synthesis and catalytic activities of pure and Cu-doped zinc oxide nanoparticles. Ebin B, editor, *Cogent Chem.*, 2017, **3**(1), 1301241, DOI: **10.1080/23312009.2017.1301241**.

32 A. Esbergenova, M. Hojamberdiev, S. Mamatkulov, R. Jalolov, D. Kong and O. Ruzimuradov, *et al.*, Correlating Cu dopant concentration, optoelectronic properties, and photocatalytic activity of ZnO nanostructures: experimental and theoretical

insights, *Nanotechnology*, 2024, **35**(48), 485701, DOI: **10.1088/1361-6528/ad750b**.

33 S. Muthukumaran and R. Gopalakrishnan, Structural, FTIR and photoluminescence studies of Cu doped ZnO nanopowders by co-precipitation method, *Opt. Mater.*, 2012, **34**(11), 1946–1953. Available from: **https://www.sciencedirect.com/science/article/pii/S0925346712002686**.

34 M. Pal, U. Pal, J. M. G. Y. Jiménez and F. Pérez-Rodríguez, Effects of crystallization and dopant concentration on the emission behavior of TiO2:Eu nanophosphors, *Nanoscale Res. Lett.*, 2012, **7**(1), 1, DOI: **10.1186/1556-276X-7-1**.

35 I. Munaweera and M. L. C. Madhusha, *Characterization Techniques for Nanomaterials*, CRC Press, Boca Raton, 2023.

36 F. J. Humphreys and M. G. Ardakani, Grain boundary migration and Zener pinning in particle-containing copper crystals, *Acta Mater.*, 1996, **44**(7), 2717–2727. Available from: **https://www.sciencedirect.com/science/article/pii/1359645495004211**.

37 E. Ahmad, M. Ullah, A. Rana, A. S. Malik, M. Farooq and I. Ahmad, *et al.*, Impact of Copper Doping on the Structural, Electrical and Optical Properties of Auto-Combustion Synthesized ZnO Nanocomposites, *Acta Phys. Pol., A*, 2019, **135**, 458–466.

38 E. I. Naik, H. S. B. Naik, B. E. K. Swamy, R. Viswanath, I. K. S. Gowda and M. C. Prabhakara, *et al.*, Influence of Cu doping on ZnO nanoparticles for improved structural, optical, electrochemical properties and their applications in efficient detection of latent fingerprints, *Chem. Data Collect.*, 2021, **33**, 100671. Available from: **https://www.sciencedirect.com/science/article/pii/S2405830021000252**.

39 G. Xiong, U. Pal, J. G. Serrano, K. B. Ucer and R. T. Williams, Photoluminesence and FTIR study of ZnO nanoparticles: the impurity and defect perspective, *Phys. Status Solidi C*, 2006, **3**(10), 3577–3581. Available from: **https://onlinelibrary.wiley.com/doi/abs/10.1002/pssc.200672164**.

40 J. S. Alzahrani, I. H. Midala, H. M. Kamari, N. M. Al-Hada, C. K. Tim and N. N. S. Nidzam, *et al.*, Effect of Calcination Temperature on the Structural and Optical Properties of $(ZnO)_{0.8}$ $(ZrO_2)_{0.2}$ Nanoparticles, *J. Inorg. Organomet. Polym. Mater.*, 2022, **32**, 1755–1765.

41 Z. Kayani, F. Saleemi and I. Batool, Effect of calcination temperature on the properties of ZnO nanoparticles, *Appl. Phys. A: Mater. Sci. Process.*, 2015, **119**, 713–720.

42 A. Mahmoud, M. Echabaane, K. Omri, J. Boudon, L. Saviot and N. Millot, *et al.*, Cu-Doped ZnO Nanoparticles for Non-Enzymatic Glucose Sensing, *Molecules*, 2021, **26**(4), 929. Available from: **https://www.mdpi.com/1420-3049/26/4/929**.

43 J. Vasudevan, S. Johnson Jeyakumar, B. Arunkumar, M. Jothibas, A. Muthuvel and S. Vijayalakshmi, Optical and magnetic investigation of Cu doped ZnO nanoparticles synthesized by solid state method, *Mater. Today: Proc.*, 2022, **48**, 438–442. Available from: **https://www.sciencedirect.com/science/article/pii/S2214785320401464**.

44 S. Singhal, J. Kaur, T. Namgyal and R. Sharma, Cu-doped ZnO nanoparticles: Synthesis, structural and electrical properties, *Phys. B*, 2012, **407**(8), 1223–1226. Available from: **https://www.sciencedirect.com/science/article/pii/S0921452612001196**.

45 N. Pradhan, S. Das Adhikari, A. Nag and D. D. Sarma, Luminescence, Plasmonic, and Magnetic Properties of Doped Semiconductor Nanocrystals, *Angew. Chem., Int. Ed.*, 2017, **56**(25), 7038–7054, DOI: **10.1002/anie.201611526**.

46 P. Y. Yu and M. Cardona, *Fundamentals of Semiconductors: Physics and Materials*, 2010. Available from: **https://app.dimensions.ai/details/publication/pub.1043423180**.

47 K. G. Saw, N. M. Aznan, F. K. Yam, S. S. Ng and S. Y. Pung, New Insights on the Burstein-Moss Shift and Band Gap Narrowing in Indium-Doped Zinc Oxide Thin Films, *PLoS One*, 2015, **10**(10), e0141180. Available from: **https://app.dimensions.ai/details/publication/pub.1031278594**.

48 J. Dai, Z. Suo, Z. Li and S. Gao, Effect of Cu/Al doping on electronic structure and optical properties of ZnO, *Results Phys.*, 2019, **15**, 102649. Available from: **https://www.sciencedirect.com/science/article/pii/S2211379719318832**.

49 B. K. Das, T. Das, K. Parashar, A. Thirumurugan and S. K. S. Parashar, Structural, bandgap tuning and electrical properties of Cu doped ZnO nanoparticles synthesized by mechanical alloying, *J. Mater. Sci.: Mater. Electron.*, 2017, **28**(20), 15127–15134, DOI: **10.1007/s10854-017-7388-2**.

50 A. J. Reddy, M. K. Kokila, H. Nagabhushana, R. P. S. Chakradhar, C. Shivakumara and J. L. Rao, *et al.*, Structural, optical and EPR studies on ZnO:Cu nanopowders prepared via low temperature solution combustion synthesis, *J. Alloys Compd.*, 2011, **509**(17), 5349–5355. Available from: **https://www.sciencedirect.com/science/article/pii/S0925838811003604**.

51 M. Sajjad, I. Ullah, M. I. Khan, J. Khan, M. Y. Khan and M. T. Qureshi, Structural and optical properties of pure and copper doped zinc oxide nanoparticles, *Results Phys.*, 2018, **9**, 1301–1309. Available from: **https://www.sciencedirect.com/science/article/pii/S2211379718303127**.

52 Z. M. Gibbs, A. LaLonde and G. J. Snyder, Optical band gap and the Burstein–Moss effect in iodine doped PbTe using diffuse reflectance infrared Fourier transform spectroscopy, *New J. Phys.*, 2013, **15**(7), 75020, DOI: **10.1088/1367-2630/15/7/075020**.

53 A. Ghosh, D. N. Kumari and A. Bhattacharjee, Investigation on structural and optical properties of Cu doped ZnO, *J. Nanosci. Nanotechnol.*, 2014, 485–489.

54 E. Burstein, Anomalous Optical Absorption Limit in InSb, *Phys. Rev.*, 1954, **93**(3), 632–633.

55 D. C. Agarwal, U. B. Singh, S. Gupta, R. Singhal, P. K. Kulriya and F. Singh, *et al.*, Enhanced room temperature ferromagnetism and green photoluminescence in Cu doped ZnO thin film synthesised by neutral beam sputtering, *Sci. Rep.*, 2019, **9**(1), 6675.

56 Z. Ma, F. Ren, X. Ming, Y. Long and A. A. Volinsky, Cu-doped ZnO electronic structure and optical properties studied by first-principles calculations and experiments, *Materials*, 2019, **12**(1), 196.

57 K. V. Chandekar, M. Shkir, B. M. Al-Shehri, S. AlFaify, R. G. Halor and A. Khan, *et al.*, Visible light sensitive Cu doped ZnO: Facile synthesis, characterization and high photocatalytic response, *Mater. Charact.*, 2020, **165**, 110387.

58 I. Aadnan, O. Zegaoui, A. El Mragui, H. Moussout and J. C. G. Esteves da Silva, Structural, optical and photocatalytic

properties under UV-A and visible lights of Co–, Ni- and Cu-doped ZnO nanomaterials. Comparative study, *Arabian J. Chem.*, 2024, **17**(1), 105336.

59 V. Pasindu and I. Munaweera, Harnessing atomic-scale defect engineering in 2D photocatalysts: synergistic integration of nanocomposite architectures for bandgap tuning and charge transfer optimization, *RSC Adv.*, 2025, **15**(41), 34191–34210, DOI: **10.1039/d5ra05074j**.

60 P. K. Labhane, V. R. Huse, L. B. Patle, A. L. Chaudhari and G. H. Sonawane, Synthesis of Cu Doped ZnO Nanoparticles: Crystallographic, Optical, FTIR, Morphological and Photocatalytic Study, *J. Mater. Sci. Chem. Eng.*, 2015, **3**(7), 13, DOI: **10.4236/msce.2015.37005**.

61 G. Byzynski, C. Melo, D. P. Volanti, M. M. Ferrer, A. F. Gouveia and C. Ribeiro, *et al.*, The interplay between morphology and photocatalytic activity in ZnO and N-doped ZnO crystals, *Mater. Des.*, 2017, **120**, 363–375. Available from: **https://www.sciencedirect.com/science/article/pii/S026412751730148X**.

62 J. Cui and U. J. Gibson, Enhanced Nucleation, Growth Rate, and Dopant Incorporation in ZnO Nanowires, *J. Phys. Chem. B*, 2005, **109**(46), 22074–22077, DOI: **10.1021/jp054160e**.

63 A. Matei, V. Țucureanu, M. C. Popescu, C. Romanițan and I. Mihalache, Influence of Cu dopant on the morpho-structural and optical properties ZnO nanoparticles, *Ceram. Int.*, 2019, **45**(8), 10826–10833. Available from: **https://www.sciencedirect.com/science/article/pii/S0272884219304596**.

64 M. R. Hoffmann, S. T. Martin, W. Choi and D. W. Bahnemann, Environmental Applications of Semiconductor Photocatalysis, *Chem. Rev.*, 1995, **95**(1), 69–96, DOI: **10.1021/cr00033a004**.

65 A. Fujishima, X. Zhang and D. Tryk, TiO2 photocatalysis and related surface phenomena, *Surf. Sci. Rep.*, 2008, **63**(12), 515–582.

66 D. Chatterjee and S. Dasgupta, Visible light induced photocatalytic degradation of organic pollutants, *J. Photochem. Photobiol., C*, 2005, **6**(2), 186–205. Available from: **https://www.sciencedirect.com/science/article/pii/S1389556705000316**.

67 V. Pasindu, P. Yapa, S. Dabare and I. Munaweera, Multifunctional transition metal oxide/graphene oxide nanocomposites for catalytic dye degradation, renewable energy, and energy storage applications, *RSC Adv.*, 2025, **15**(40), 33162–33186, DOI: **10.1039/d5ra04806k**.

68 H. A. H. Alzahrani, Y. Q. Almulaiky and A. O. Alsaiari, The photocatalytic dye degradation of methylene blue (MB) by nanostructured ZnO under UV irradiation, *Phys. Scr.*, 2023, **98**(4), 045703. Available from: **https://app.dimensions.ai/details/publication/pub.1155686148**.

69 D. Blažeka, R. Radičić, D. Maletić, S. Živković, M. Momčilović and N. Krstulović, Enhancement of Methylene Blue Photodegradation Rate Using Laser Synthesized Ag-Doped ZnO Nanoparticles, *Nanomaterials*, 2022, **12**(15), 2677. Available from: **https://www.mdpi.com/2079-4991/12/15/2677**.

70 A. Lins, A. G. Jerônimo, R. Barbosa, L. Neves, P. Trigueiro and L. C. Almeida, *et al.*, Facile Synthesis of Ni-Doped ZnO Nanoparticles Using Cashew Gum: Investigation of the Structural, Optical, and Photocatalytic Properties, *Molecules*, 2023, **28**(23), 7772. Available from: **https://www.mdpi.com/1420-3049/28/23/7772**.

71 T. Imboon, K. Sugio, J. Khumphon, L. Sridawong, V. Mangala Gowri and K. Yamada, *et al.*, Synergistic Effects of Fe-Doped ZnO and Graphene Oxide for Enhanced Photocatalytic Performance and Tunable Magnetic Properties, *ACS Omega*, 2025, **10**(31), 34571–34587, DOI: **10.1021/acsomega.5c03213**.

72 G. Chen, M. Yang, B. Tian, J. Yao, S. Chen and D. Li, *et al.*, Cu-doped ZnO nanoparticles and its application for the photocatalytic degradation of Rhodamine B, *Sci. Rep.*, 2025, **15**(1), 18246, DOI: **10.1038/s41598-025-02432-x**.

73 K. Ranathunga, P. Yapa, I. Munaweera, M. M. Weerasekera and C. Sandaruwan, Preparation and characterization of Fe-ZnO cellulose-based nanofiber mats with self-sterilizing photocatalytic activity to enhance antibacterial applications under visible light, *RSC Adv.*, 2024, **14**(26), 18536–18552.

74 W. Brand-Williams, M. E. Cuvelier and C. Berset, Use of a free radical method to evaluate antioxidant activity, *LWT – Food Sci. Technol.*, 1995, **28**(1), 25–30.

75 K. Omri, A. Bettaibi, K. Khirouni and L. El Mir, The optoelectronic properties and role of Cu concentration on the structural and electrical properties of Cu doped ZnO nanoparticles, *Phys. B*, 2018, **537**, 167–175. Available from: **https://www.sciencedirect.com/science/article/pii/S0921452618301443**.

76 C. A. Marin-Flores, O. Rodríguez-Nava, M. García-Hernández, R. Ruiz-Guerrero, F. Juárez-López and A. de Jesús Morales-Ramírez, Free-radical scavenging activity properties of ZnO sub-micron particles: size effect and kinetics, *J. Mater. Res. Technol.*, 2021, **13**, 1665–1675. Available from: **https://www.sciencedirect.com/science/article/pii/S2238785421004907**.

77 Y. K. Mohanta, S. K. Panda, R. Jayabalan, N. Sharma, A. K. Bastia and T. K. Mohanta, Antimicrobial, Antioxidant and Cytotoxic Activity of Silver Nanoparticles Synthesized by Leaf Extract of Erythrina suberosa (Roxb.), *Front. Mol. Biosci.*, 2017, **4**, 14. Available from: **https://www.frontiersin.org/journals/molecular-biosciences/articles/10.3389/fmolb.2017.00014**.

78 S. B. Kedare and R. P. Singh, Genesis and development of DPPH method of antioxidant assay, *J. Food Sci. Technol.*, 2011, **48**, 412–422, DOI: **10.1007/s13197-011-0251-1**.

79 Z. Yu, Q. Li, J. Wang, Y. Yu, Y. Wang, Q. Zhou and P. Li, Reactive Oxygen Species-Related Nanoparticle Toxicity in the Biomedical Field, *Nanoscale Res. Lett.*, 2020, **15**(1), 115.

80 A. A. Aly and M. K. Ahmed, Nanofibers of cellulose acetate containing ZnO nanoparticles/graphene oxide for wound healing applications, *Int. J. Pharm.*, 2021, **598**, 120325.

81 S. Ghosh, S. Vaidya, N. More, R. Velyutham and G. Kapusetti, Piezoelectric-based bioactive zinc oxide-cellulose acetate electrospun mats for efficient wound healing: an in vitro insight, *Front. Immunol.*, 2023, **14**, 1245343.

82 I. S. Okeke, K. K. Agwu, A. A. Ubachukwu and F. I. Ezema, Influence of transition metal doping on physiochemical and

antibacterial properties of ZnONanoparticles: A review, *Appl. Surf. Sci. Adv.*, 2022, **8**, 100227. Available from: **https://www.sciencedirect.com/science/article/pii/S2666523922000198**.

83 B. Qu, Z. Xiao and Y. Luo, Sustainable nanotechnology for food preservation: Synthesis, mechanisms, and applications of zinc oxide nanoparticles, *J. Agric. Food Res.*, 2025, **19**, 101743. Available from: **https://www.sciencedirect.com/science/article/pii/S2666154325001140**.

84 R. O. Asriza, R. Ropalia, D. Humaira, G. O. Ryaldi and Zomi, Characterization of cellulose acetate functional groups synthesized from corn husk (Zea mays), *IOP Conf. Ser. Earth Environ. Sci.*, 2021, **926**(1), 12060, DOI: **10.1088/1755-1315/926/1/012060**.

85 M. Ibrahim, T. Fahmy, E. Salaheldin, F. Mobarak, M. Youssef and M. Mabrook, Role of Tosyl Cellulose Acetate as Potential Carrier for Controlled Drug Release, *Life Sci. J.*, 2015, **12**, 127–133.

86 C. Voorhis, J. González-Benito and A. Kramar, ''Nano in Nano''—Incorporation of ZnO Nanoparticles into Cellulose Acetate–Poly(Ethylene Oxide) Composite Nanofibers Using Solution Blow Spinning, *Polymers*, 2024, **16**(3), 341. Available from: **https://www.mdpi.com/2073-4360/16/3/341**.

87 I. Munaweera and M. L. C. Madhusha, *Smart Nanomaterials*, CRC Press, Boca Raton, 2023.

88 İ. Gulcin and S. H. Alwasel, DPPH Radical Scavenging Assay, *Processes*, 2023, **11**(8), 2248. Available from: **https://www.mdpi.com/2227-9717/11/8/2248**.

89 M. D. M. Rahman, M. D. B. Islam, M. Biswas and A. H. M. Khurshid Alam, In vitro antioxidant and free radical scavenging activity of different parts of Tabebuia pallida growing in Bangladesh, *BMC Res. Notes*, 2015, **8**(1), 621, DOI: **10.1186/s13104-015-1618-6**.

90 M. M. Ibrahim, T. Y. A. Fahmy, E. I. Salaheldin, F. Mobarak, M. A. Youssef and M. R. Mabrook, Role of tosyl cellulose acetate as potential carrier for controlled drug release, *Life Sci. J.*, 2015, **12**(10), 127–133.

91 S. D. Deshapriya and I. Munaweera, Visible-Light-Active Electrospun Membranes Based on Cobalt-Doped ZnO Nanohybrids: Applications for Food Packaging, *ChemistrySelect*, 2024, **9**(9), e202303830.

92 A. Khalid, P. Ahmad, A. I. Alharthi, S. Muhammad, M. U. Khandaker and M. Rehman, *et al.*, Structural, Optical, and Antibacterial Efficacy of Pure and Zinc-Doped Copper Oxide Against Pathogenic Bacteria, *Nanomaterials*, 2021, **11**(2), 451. Available from: **https://www.mdpi.com/2079-4991/11/2/451**.

93 Y. Li, C. Liao and S. C. Tjong, Recent Advances in Zinc Oxide Nanostructures with Antimicrobial Activities, *Int. J. Mol. Sci.*, 2020, **21**(22), 8836. Available from: **https://www.mdpi.com/1422-0067/21/22/8836**.